UC Irvine
UC Irvine Electronic Theses and Dissertations

Title
Advances in the Direct Spectral Estimation of Acoustic Sources Using Continuous-Scan Phased Arrays

Permalink
https://escholarship.org/uc/item/8xm5w89k

Author
Morata Carranza, David

Publication Date
2019

Copyright Information
This work is made available under the terms of a Creative Commons Attribution-NonCommercial License, availalbe at https://creativecommons.org/licenses/by-nc/4.0/

Peer reviewed|Thesis/dissertation

eScholarship.org Powered by the California Digital Library
University of California

UNIVERSITY OF CALIFORNIA,
IRVINE

Advances in the Direct Spectral Estimation of Acoustic Sources Using Continuous-Scan Phased Arrays

THESIS

submitted in partial fulfillment of the requirements
of the degree of

MASTER OF SCIENCE

in Mechanical and Aerospace Engineering

by

David Morata Carranza

Thesis Committee:
Professor Dimitri Papamoschou, Chair
Professor Roger H. Rangel
Professor Tryphon Georgiou

2019

© 2019 David Morata Carranza

TABLE OF CONTENTS

Page

LIST OF FIGURES **iv**

LIST OF TABLES **viii**

NOMENCLATURE **ix**

ACKNOWLEDGMENTS **xi**

ABSTRACT OF THE THESIS **xii**

1 Introduction **1**
1.1 Motivation 1
1.2 Components of Jet Noise 4
1.3 Acoustic Imaging Techniques 8
1.4 Previous Work 11
1.5 Thesis Overview 13

2 Background **14**
2.1 Model for the acoustic field 14
2.2 Inversion Methods 23

3 Block distribution **27**
3.1 Maximum block length 27
3.2 Minimum block length 31
3.3 Selection of the number of blocks 34
3.4 Width of the frequency-dependent window 36
3.5 Optimal block configurations 39

4 Experimental setup **42**
4.1 Phased Microphone Array 42
4.2 Determination of the Position of the Scanning Sensor 46
4.3 Block distribution 49
4.4 Array Configurations 50
4.4.1 Full Array Configuration 51
4.4.2 Partial Array Configuration 55
4.5 Noise Sources 58

4.6 Sound Pressure Level and Overall Sound Pressure Level 60

5 Results **62**
5.1 Sound Pressure Level 62
5.1.1 Impinging Jets Source 62
5.1.2 Overexpanded Jet 65
5.2 Acoustic Source Maps 67
5.2.1 Impinging Jets Source 67
5.2.2 Overexpanded Jet 73

6 Conclusion **83**
6.1 Summary 83
6.2 Recommendations for Future Work 84

Bibliography **86**

LIST OF FIGURES

Page

1.1 Housing value loss in communities in the surroundings an airport. Figure extracted from Kish.[3] 2
1.2 (a) Spark schlieren image of an overexpanded jet tested in the UCI aeroacoustics facility. (b) Blackbird (image from the U.S. Air Force) 5
1.3 Far-field supersonic jet noise spectrum of an overexpanded jet tested in the UCI aeroacoustics facility. Microphone placed at 70.65° to the nozzle inlet direction. 6
1.4 Schematic of a microphone phased array. 9

2.1 Schematic of a line source distribution 15
2.2 Segmentation of the pressure signal for sensors m and n into K blocks. . . . 17
2.3 Example of the frequency-dependent windowing of the signal within a given block at a fixed frequency. The blue curve represents the Gaussian envelope $g(t, \omega)$ while the grey curve represents a random signal. 21
2.4 Illustration of the independent elements (bold) of the coherence matrices arising from $M_f = 4$ fixed sensors and $M_s = 2$ scanning sensors. Colored areas indicate the elements that vary from one block to the next. Off-diagonal elements comprise real and imaginary components. Diagonal elements are all equal to 1. 24

3.1 Subscript convention for the faces of the block. Letter U corresponds to the upstream facing end (marked in green), letter D corresponds to the downstream face (marked in red) and letter C corresponds to the center of the block (marked in blue). 29
3.2 Sound Pressure Level difference between consecutive segment pairs. 33
3.3 Example of the envelope showing the number of blocks versus the block length 35
3.4 Example of frequency-dependent Gaussian window for two frequencies on a given pressure signal. (a) Shape of the Gaussian envelope; (b) Pressure signal multiplied by the Gaussian envelope for a frequency of 10 kHz; (c) Pressure signal multiplied by the Gaussian envelope for a frequency of 90 kHz; 37
3.5 Example of the unused block size due to the effect of the frequency-dependent Gaussian window. 38
3.6 Example of the optimal regions as a function of block size and number of blocks. 40
3.7 Sketch of the compromise solution that is adopted relating the size of the FFT, the number of blocks and the block length with the frequency. 41

4.1 Anechoic chamber. 43
4.2 Design of the linear traverse system. 44
4.3 Fixed and scanning microphones at their closest spacing of 6mm, measured from the cartridge centers. 44
4.4 Example of the synchronization of the microphone traces with the position. (a) Pressure signal $p(t)$; (b) Synchronization signal 47
4.5 Laser-based distance measurement system. 47
4.6 Voltage divider used to condition the signal output of the SICK laser-based displacement sensor. 48
4.7 Scanning microphone trajectory comparison for experiment "JET0271". . . . 49
4.8 Array configurations showing the fixed sensors only. The figure on the top corresponds to the full array configuration (12 fixed sensors) while the image on the bottom is the partial array configuration (5 fixed sensors). 51
4.9 Full array with the base block configuration (35 block). Scanning sensor is shown at the block center times t_k. 52
4.10 Distance histogram for the full microphone array using the 35 block configuration. The position at the block center time t_k is used when the scanning sensor is involved. The image on the left is the complete distance histogram. The image on the right shows a detail of the small distances of the histogram. 53
4.11 Distance histogram for the full microphone array using; (a) the 120 block configuration; (b) the 242 block configuration. For plots (a) and (b) the image on the left is the complete distance histogram. The image on the right shows a detail of the small distances of the histogram. 53
4.12 Distance histogram for the full microphone array using; (a) the 436 block configuration; (b) the 919 block configuration. For plots (a) and (b) the image on the left is the complete distance histogram. The image on the right shows a detail of the small distances of the histogram. 54
4.13 Full array with the base block configuration (35 block). Scanning sensor is shown at the block center times t_k. 55
4.14 Distance histogram for the sparse microphone array using the 35 block configuration. The position at the block center time t_k is used when the scanning sensor is involved. The image on the left is the complete distance histogram. The image on the right shows a detail of the small distances of the histogram. 56
4.15 Distance histogram for the sparse microphone array using; (a) the 120 block configuration; (b) the 242 block configuration. For plots (a) and (b) the image on the left is the complete distance histogram. The image on the right shows a detail of the small distances of the histogram. 56
4.16 Distance histogram for the sparse microphone array using; (a) the 436 block configuration; (b) the 919 block configuration. For plots (a) and (b) the image on the left is the complete distance histogram. The image on the right shows a detail of the small distances of the histogram. 57
4.17 Radial coordinates of the nozzle and plate. The plate at the nozzle exit enhances the feedback mechanism loop. 58
4.18 Image of the convergent-divergent nozzle with annular end plate. 59
4.19 Impinging jets source. 59

5.1 Overall Sound Pressure Level for the Impinging Jets Source. 63
5.2 SPL spectra for the impinging jets source at different polar angles. The polar angles are, from left to right: $\theta = 48.2°$; $\theta = 50.38°$; $\theta = 54.17°$; $\theta = 58.37°$. . 63
5.3 SPL spectra for the impinging jets source at different polar angles. The polar angles are, from left to right: $\theta = 62.98°$; $\theta = 68.00°$; $\theta = 70.65°$; $\theta = 73.40°$. 64
5.4 Overall Sound Pressure Level Overexpanded Jet. 65
5.5 SPL spectra for the overexpanded jet at different polar angles. The polar angles are, from left to right: $\theta = 48.2°$; $\theta = 50.38°$; $\theta = 54.17°$; $\theta = 58.37°$. . 66
5.6 SPL spectra for the overexpanded jet at different polar angles. The polar angles are, from left to right: $\theta = 62.98°$; $\theta = 68.00°$; $\theta = 70.65°$; $\theta = 73.40°$. 66
5.7 Coherence-based source strength $\psi(x, \omega)$ for the Impinging Jets Source using the full array configuration with the signal segmentation of Ref. 1. (a) Delay-and-sum (F12); (b) Bayesian estimation (F12); (c) Bayesian estimation (F11S01). 68
5.8 Coherence-based source strength $\psi(x, \omega)$ for the Impinging Jets Source using the full array configuration. (a) Bayesian estimation (F11S01) with the baseline block distribution of Ref. 1; (b) Bayesian estimation (F11S01) with the proposed block distribution. 69
5.9 Measured coherence of the acoustic field for the Impinging Jets Source experiment as a function of the distance. 70
5.10 Coherence-based source strength $\psi(x, \omega)$ for the Impinging Jets Source using the partial array configuration with the signal segmentation of Ref. 1. (a) Delay-and-sum (F05); (b) Bayesian estimation (F05); (c) Bayesian estimation (F04S01). 71
5.11 Coherence-based source strength $\psi(x, \omega)$ for the Impinging Jets Source using the full array configuration. (a) Bayesian estimation (F04S01) with the baseline block distribution of Ref. 1; (b) Bayesian estimation (F04S01) with the proposed block distribution. 72
5.12 Coherence-based source strength $\psi(x, \omega)$ for the overexpanded jet using the full array configuration. (a) Delay-and-sum (F12); (b) Bayesian estimation (F12); (c) Bayesian estimation (F11S01) 74
5.13 Detail of the coherence-based source strength $\psi(x, \omega)$ for the overexpanded jet using the full array configuration with the baseline block distribution of Ref. 1. (a) Delay-and-sum (F12); (b) Bayesian estimation (F12); (c) Bayesian estimation (F11S01) with the baseline block distribution. 75
5.14 Coherence-based source strength $\psi(x, \omega)$ for the overexpanded jet using the full array configuration. (a) Bayesian estimation (F11S01) with the baseline block distribution of Ref. 1; (b) Bayesian estimation (F11S01) with the proposed block distribution. 76
5.15 Detail of the coherence-based source strength $\psi(x, \omega)$ for the overexpanded jet using the full array configuration for the high frequencies. (a) Bayesian estimation (F11S01) with the baseline block distribution of Ref. 1; (b) Bayesian estimation (F11S01) with the proposed block distribution. 77
5.16 Measured coherence of the acoustic field for the Impinging Jets Source experiment as a function of the distance. 77

5.17 Detail of the coherence-based source strength $\psi(x, \omega)$ for the overexpanded jet using the full array configuration. (a) Delay-and-sum (F05); (b) Bayesian estimation (F05); (c) Bayesian estimation (F04S01) with the block distribution of Ref. 1 78
5.18 Detail of the coherence-based source strength $\psi(x, \omega)$ for the overexpanded jet using the full array configuration. (a) Delay-and-sum (F05); (b) Bayesian estimation (F05); (c) Bayesian estimation (F04S01) with the block distribution of Ref. 1 79
5.19 Coherence-based source strength $\psi(x, \omega)$ for the overexpanded jet using the partial array configuration. (a) Bayesian estimation (F04S01) with the baseline signal segmentation of Ref. 1; (b) Bayesian estimation (F04S01) with the proposed signal segmentation. 80
5.20 Detail of the coherence-based source strength $\psi(x, \omega)$ for the overexpanded jet using the partial array configuration for the high frequencies. (a) Bayesian estimation (F04S01) with the baseline block distribution of Ref. 1; (b) Bayesian estimation (F04S01) with the proposed block distribution. 81
5.21 Detail of the coherence-based source strength $\psi(x, \omega)$ for the overexpanded jet.(a) Bayesian estimation (F11S01) with the baseline block distribution of Ref. 1; (b) Bayesian estimation (F11S01) with the proposed block distribution; (c) Bayesian estimation (F04S01) with the proposed block distribution 82

LIST OF TABLES

Page

4.1 Summary of data acquisition parameters. 45
4.2 Summary of the different block distributions used in earlier work (Ref 1). . . 50
4.3 Summary of the different block distributions of the signal processing developed in this work. 50

NOMENCLATURE

Roman Symbols

ℓ	source-sensor distance
a	speed of sound
c	coefficient
D	jet diameter
f	cyclic frequency
G	cross-spectral matrix
g	frequency-dependent window
K	number of blocks
M	number of microphones
N	length of frequency vector
N_{FFT}	size of Fast Fourier Transform
p	pressure fluctuation
r	radial distance
S	number of segments in a block
Sr	Strouhal number= fD/U
T	block duration
t	time
U	fully-expanded jet velocity
V	sensor speed
x	axial coordinate
y	transverse coordinate

Z	array response matrix

Greek Symbols

β	Doppler factor (Eq. 2.7)
δ	width of Gaussian window
θ	polar angle relative to jet axis
Θ	directivity matrix
λ	acoustic wavelength
ξ	axial coordinate; virtual coordinate in Bayesian estimation
ψ	coherence-based source distribution
Φ	spectrum-based source distribution
τ	source-sensor time; time separation in correlations
ω	angular frequency
ω'	Doppler-shifted frequency
ω''	frequency of spectral oscillation
σ	block overlap; segment overlap

Subscripts

μ	scanning sensor index
f	fixed sensor
k	block index
m	microphone index
n	microphone index; frequency index
s	segment index; scanning sensor

Acronyms

FFT	Fast Fourier Transform
SPL	Sound Pressure Level
WVS	Wigner-Ville Spectrum
XWVS	Cross Wigner-Ville Spectrum

ACKNOWLEDGMENTS

I would like to thank Professor Dimitri Papamoschou for the great opportunity to work in the engaging field of aeroacoustics. His expertise and enthusiasm have motivated me in this journey and he has provided me a very valuable learning experience. I appreciate all of his guidance and support, not only in my research work but in the classes that I have taken with him.

I want to thank the members of the Thesis Committee, Professor Roger Rangel and Professor Tryphon Georgiou. They have been very supportive all this time that I have been at UCI.

I extend my gratitude to Mr. Pete Balsells for establishing the Balsells Foundation and starting this wonderful Fellowship, and to all the people that make it work including Professor Roger Rangel, Generalitat de Catalunya and the University of California-Irvine.

A special thank goes to the Balsells Fellows with whom I have been able to share memorable experiences.

Finally, a special thank to my parents, Cori and Sisco, to my brother, Pau, and Shail, who have given me endless encouragement, support and, most importantly, love.

This work was conducted with NASA Phase I and Phase II SBIR funding (contracts NNX16CC79P and NNX17CC18C) under technical monitor of Dr. David Stephens. Their support is greatly appreciated.

Parts of this work are a review of the journal paper by D. Papamoschou, P. Shah and myself, titled "Inverse Acoustic Methodology for Continuous-Scan Phased Arrays".[1] The work was first presented as a conference paper[2] in the AIAA Aviation Conference held in Atlanta, on June 2018.

ABSTRACT OF THE THESIS

Advances in the Direct Spectral Estimation of Acoustic Sources Using Continuous-Scan Phased Arrays

By

David Morata Carranza

Master of Science in Mechanical and Aerospace Engineering

University of California, Irvine, 2019

Professor Dimitri Papamoschou, Chair

The present study is related to the field of imaging of aeroacoustic noise sources. Traditional techniques include the use of phased microphone arrays and acoustic beamforming of the signals signals using algorithms such as the Delay-And-Sum (DAS) method. Over the last years, there has been an increasing interest in methods in which some of the sensors traverse in prescribed paths and motion. Some of the challenges of this approach include the treatment of the non-stationarity of the signal due to the motion of the microphone(s).

An objective of this work is to review the methodology presented by D. Papamoschou, P. Shah and myself in the AIAA Journal paper[1] since it provides the building grounds for the thesis. The methodology accounts for the direct estimation of the spatio-spectral distribution of an acoustic source from microphone measurements that include fixed and continuously scanning sensors. The non-stationarity of the signal is addressed by means of the Wigner-Ville spectrum. Suppression of the non-stationary effects involves the division of the signal into blocks and the application of a frequency-dependent window within each block. The direct estimation approach involves the inversion of an integral that relates the modeled pressure field, the measured pressure field and the response of the array. A

Bayesian-estimation that allows for efficient inversion of the integrals and performs similarly to the conjugate gradient method is reviewed.

The coherence-based noise source distribution is studied in this work and the influence of the signal segmentation on its correct resolution is analyzed. This thesis provides specific guidelines related to the signal processing. The signal is divided into blocks meeting a desired mathematical condition. A minimum and maximum size for the resulting blocks is proposed in this work, as well as a minimum and maximum block overlap. A safe region for the signal segmentation is presented as well.

This work presents a methodology to synchronize the signals from the microphones (scanning or not) with the position of the scanning sensor. It also shows the methods to check the accuracy of the position scanning sensor.

The methodology is applied to acoustic fields emitted by impinging jets approximating a point source and an overexpanded supersonic jet. Noise source maps that included the scanning sensor and a dense block distribution have increased spatial resolution and reduced sidelobes. The ability of the continuous scan paradigm to provide high-definition noise source maps with a lower sensor count is confirmed in this work as well. The effect of the proposed signal segmentation on sparse arrays is discussed.

Chapter 1

Introduction

1.1 Motivation

Research on aircraft noise has engaged the industry and the academia for more than 60 years. It has gained more attention during the last two decades as people have become more aware of the negative health impacts of noise produced by air transportation. At the time being, there is strong concern about the maximum noise levels that the communities can accommodate without presenting health, environmental and economic risks. Such communities are more vulnerable when they are in the proximity of an airport. Some examples of health complications caused by prolonged exposure to aircraft noise include cognitive impacts on children, annoyance or sleep disturbance. Housing devaluation, restrictions on airline schedules and penalties for exceeding the noise limits are some illustrations of the economic impacts of excessive noise due to aircraft operations. Aircraft noise has thus become a dominant driver in the design of aircraft and their propulsion systems.

A study by Kish[3] analyzed the impacts of aviation noise of 181 airports in 38 countries and Taiwan suggesting an estimated $21 billion loss in housing value and $800 million loss in rent

during 2005 only. The same work provides an estimate of the detrimental health impacts suffered by the people that live in the neighborhoods of an airport. The study determines that 14 million residents are constantly exposed to a noise level of 55 dB (equivalent to the noise level of an electric toothbrush) and approximately 2.3 million people feel annoyed because of the excessive and continued exposure to aircraft noise. The author further indicates that without any technological or operational advance, future impacts of aviation noise could grow to $41 billion in housing value loss and $1.6 billion in rent loss per year and a major increase to 24 million people exposed to aircraft noise levels of 55 dB. These numbers would most likely increase if supersonic transportation is taken into consideration due to its, in general, louder operations.

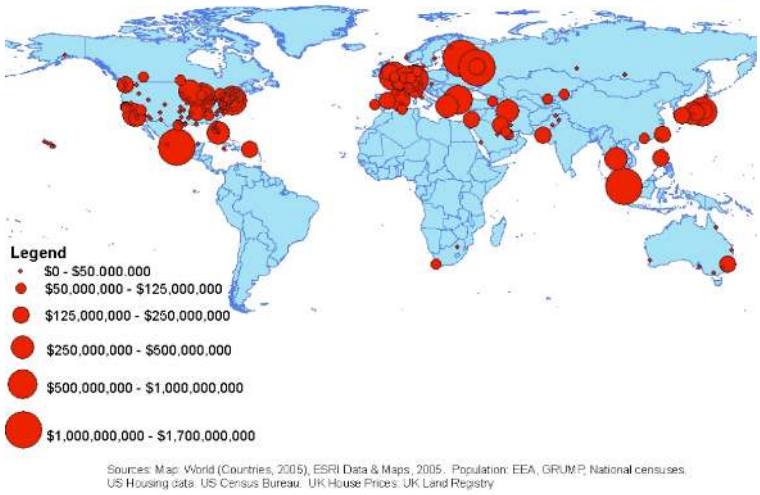

Figure 1.1: Housing value loss in communities in the surroundings an airport. Figure extracted from Kish.[3]

Air traffic is expected to double over the next two decades and there is increasing pressure to make aircraft quieter so that their noise footprint is confined to within the perimeter of the airport. The need for quieter aircraft becomes evident at this point. However, with the noise of individual airplanes having been reduced significantly in the last 20 years, further progress requires increasing sophistication in the noise detection methods.

A prevailing diagnostic for noise source detection is the microphone phased array, which combines simultaneously-acquired microphone signals to form a focused beam that measures the intensity and spatial localization of noise sources (the technique is known as beamforming). An overview and state-of-the-art of the acoustic imaging techniques is presented in next sections.

1.2 Components of Jet Noise

Jet noise is a part in aeroacoustics that concentrates on the study of noise generated by the instabilities involving the shear layer on jets and their interaction. Subsonic and supersonic jet flows contain both small-scale and large-scale turbulence playing a crucial role on noise generation. Usually, the principal noise generator in subsonic jets is the small-scale turbulence. However, supersonic jets might contain large-scale turbulence structures that have have a supersonic convective mach number (the Mach number at which the large-scale structures are convected downstream) becoming very effective noise generators. When these large-scale structures are being convected at a supersonic Mach number, they produce an energetic Mach wave radiation. This acoustic emission can quickly surpass the noise generation from the fine-scale turbulence. This work discusses the noise generated in a supersonic screeching jet and presents beamformed results of the acoustic sources. As such, a general overview of supersonic jet noise is presented next.

Supersonic jet noise consists of three components: turbulent mixing noise, screech tones and broadband shock-associated noise. The latter two appear when supersonic jets are imperfectly expanded, i.e. there is a pressure difference between the jet exit and the ambient air. The pressure mismatch originates shocks and/or expansions at the nozzle exit which cause supersonic jet noise to be very different from subsonic jet noise. These shocks and expansions usually repeat along the jet plume forming a quasi-periodic shock-cell structure, a feature also known as diamond-pattern shape. This pattern can clearly be seen on Fig 1.2.

Figure 1.3 shows a typical noise spectrum of a jet operating at off-design conditions. The image displays a very sharp peak corresponding to a screech tone of a frequency around 10 kHz. These tones are usually accompanied by its harmonics and, depending on the direction of observation, their intensity becomes stronger. The low-frequency bump corresponds to

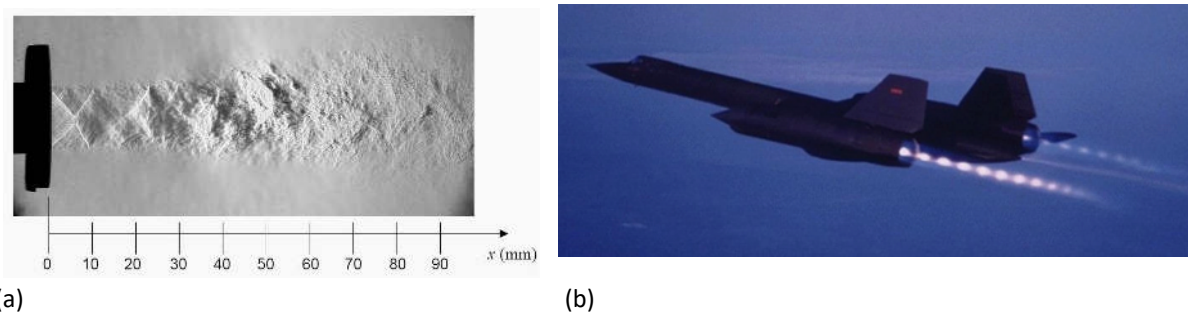

Figure 1.2: (a) Spark schlieren image of an overexpanded jet tested in the UCI aeroacoustics facility. (b) Blackbird (image from the U.S. Air Force)

the turbulent mixing noise while the broadband shock-associated noise is found to the right of the screech tone.

Screech tones are a consequence of the interaction of the shocks and the instability wave in the shear layer and were first observed by Powell in 1953.[4] They are regarded to be the consequence of a feedback loop mechanism. The amplitude of the instability wave grows and propagates downstream, interacting with the shock-cell structure of the jet (see Fig 1.2). This interaction yields to acoustic radiation in the upstream direction primarily. The feedback mechanism closes when this radiation agitates the mixing layer in the nozzle lip, as explained by Tam in his review of the supersonic jet noise.[5] Raman[6] mentions how the frequency of the screech tone and its intensity is strongly dependent on the jet Mach number, the nozzle lip thickness and the presence of surfaces close to the nozzle lip that can reflect the acoustic waves. While the fundamental screech tone has been found to radiate primarily in the upstream direction, the studies by Tam[7] and Norum[8] show how the principal direction of radiation of the first harmonic appears to be between 75° and 90° to the nozzle inlet direction. Several studies, such as the one by Verma & Rathakrishnan,[9] have found that the source of screech lies between the third and the fourth shock-cell.

The second noise component that arises as a consequence of the pressure mismatch at the nozzle exit when operating at off-desing conditions is the broadband shock-associated noise.

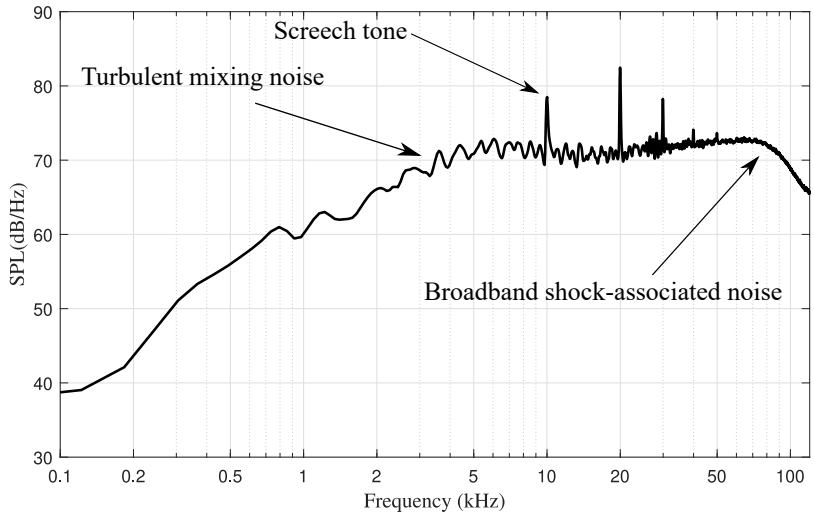

Figure 1.3: Far-field supersonic jet noise spectrum of an overexpanded jet tested in the UCI aeroacoustics facility. Microphone placed at 70.65° to the nozzle inlet direction.

This noise component has been related to the interaction between the large-scale turbulence structures of the jet and the shock-cell expansion structure.[10] Typically, the upstream directions are the most influenced by the broadband shock-associated noise as discussed by Tam.[5] The screech tones and the shock-associated noise can be eliminated if there are no shocks present on the nozzle exit (i.e. by pressure matching between the static and the ambient air pressures). Therefore, there is typically a greater focus in the reduction of turbulent mixing noise.

The turbulent mixing noise is generated by large- and the fine-scale turbulence structures of the jet flow, the former being the dominant part. In general, the principal directions of radiation are towards the downstream direction.[5] The relatively flat region near the low frequencies that exist on an imperfectly expanded jet spectrum are believed to be due to the fine-scale turbulence structure (also known as background noise). The intensity and directional characteristics of this jet noise component depend on the jet Mach number and the ratio between the jet and the ambient temperature. In supersonic jet flows, when the turbulent structures travel to the downstream direction with a supersonic Mach number, they

generate waves that propagate in the form of Mach wave radiation, as previously mentioned. The noise impact of the Mach wave radiation is usually more important than the noise generated by the fine-scale turbulence structures of the jet flow. Subsonic jets also contain fine-scale structures that are also able to generate noise. This was demonstrated by Tam *et. al.*[1112] and Viswanathan.[13]

1.3 Acoustic Imaging Techniques

The applications of acoustic beamforming can be tracked down to World War I. The book by Johnson & Dudgeon[14] presents a revealing example of real-time beamforming used by the French soldiers during that time. The text explains how the soldiers used a carefully designed array to detect approaching aircraft. The array was composed of two smaller subarrays that were distributed in a specific geometrical configuration. The sensors of each subarray were fed into an acoustic wave guide; then a listener used two equal-length ducts to redirect the sound into their ears. Because these subarrays were separated by approximately two meters, they enhanced the natural acoustic source localization that is inherent to the human ears by a factor of about ten. But more than that, since each subarray was "averaging" the signal of six acoustic sensors, the signal to noise ratio was increased significantly.

The problem of noise source localization from a collection of microphone measurements has been exhaustively studied by the scientific community since then, yielding to the invention of powerful processing techniques for acoustic source localization. Nowadays it finds applications in diverse fields such as aeroacoustics, music or speech recognition. One of the most popular diagnostic tools for acoustic source detection in aeroacoustics is the microphone phased array, which consists of a series of microphones distributed over a region of space, that are being sampled simultaneously. Traditional beamforming uses these microphone signals to form a focused beam that measures the intensity and the spatial localization of the acoustic sources. The signals are delayed and summed based on the arrival time difference. The direction of arrival (DOA) is estimated considering the geometry of the phased array and the signal delay between the sensors. This concept is the foundation of a powerful tool know as Delay-And-Sum (DAS).

Typically, the noise source image obtained with traditional beamforming techniques is a convolution between the modeled source distribution (e.g. a distribution of uncorrelated

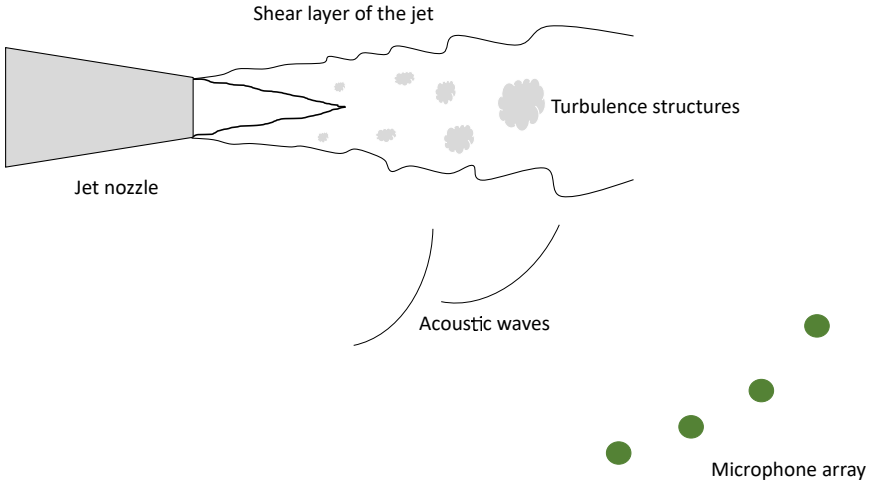

Figure 1.4: Schematic of a microphone phased array.

monopoles) and the array point spread function. The microphone array configuration can be very complex depending on its application, as shown in the paper by Sarradj[15] or Aracondoulis.[16] The array point-spread-function (PSF) relates, in general terms, how much the signal from a point source located at a given point in space x and with a characteristic frequency f is amplified or diminished because of the geometrical array configuration. There is abundant literature related to the optimal array design depending on the application. However, in some cases the beam focus might be too large to detect small sources. Additionally, traditional beamformed maps might suffer from sidelobes that are inherent to the point spread function. The combination of a coarse beam and the presence of the sidelobes might produce a blurry image, wiping out the fine characteristic details of the acoustic field. To overcome this issue and reject the sidelobes, various deconvolution approaches have been developed in the past years.

A very-well known deconvolution approach is the DAMAS (Deconvolution Approach for the Mapping of Acoustic Sources), published in 2004 by Brooks and Humphreys, from the NASA Langley Research Center. The method has been proven to be a powerful tool for the accurate quantification of the position of the acoustic source and its intensity. The

DAMAS processing aims to minimize the effect of the point spread function and de-blurry the noise source map. Later, Dougherty[17] expanded on the DAMAS algorithm and presented DAMAS2 and DAMAS3, with an increased speed of the algorithm. Yet, the computation costs of the method might become high depending on the extent of the surveyed region.

The whole "steering" approach used in traditional beamforming can be obviated by what is known as Direct Spectral Estimation (DSE). This concept is based on the reduction of the difference between a modeled pressure field and the actual pressure field that is recorded by the microphones. To this extent, Papamoschou presented a methodology to generate high-resolution noise source maps with self-consistency (integration over the source region of interest yields the far-field pressure auto-spectrum for a given emission angle).[18] The DSE approach has been shown to provide results comparable to the deconvolution of the DAS imaged of sound from turbulent jets and allows for the self-consistent treatment of more complex noise sources.

Efforts to improve the spatial resolution of the noise source maps include the experimentation with microphone arrays containing fixed and scanning sensors.

1.4 Previous Work

The continuous-scan approach used in this study can be considered as an extension of the stop-and-start method of Lee and Bolton.[19] Analogous beamforming problems involve the imaging of moving sources using fixed sensors. The continuous-scan paradigm has found applications in many different fields such as near-field holography[20,21] or order tracking.[22] Additional examples of continuous-scan beamforming are and beamforming[23] and the study by Nicolas,[24] which is applied to noise source localization of aeroacoustic sources.

The direct spectral estimation approach entails the inversion of an integral that connects the coherence of the acoustic field and the distribution of the acoustic source. It presents some advantages when compared to other traditional beamforming approaches: all sources are considered at once and interferences between potentially coherent sources can be considered. The inversion of the acoustic problem can be done by means of the conjugate gradient minimization method[25] by minimizing, in a least square sense, the difference between the modeled and the real pressure field. However, in this application the method requires a high number of calculations (calculation of the gradient in a high number of directions) making it computationally expensive. Another typical solution to overcome the ill-posed nature of the acoustic problem is to use the Tikhonov regularization, which consists of minimizing the least square error between the modeled and the actual pressure field and the norm of the source terms. However, this approach introduces a new variable that needs to be conveniently chosen known as the Tikhonov parameter.

A potential novel way of inverting the acoustic problem is by means of a Bayesian estimation. Leclere *et. al.*[26] presented an application of a Bayesian estimation method to assess the source distribution of an underexpanded screeching jet. Additional work by Pereira *et. al.*[27] presented some results of acoustic source localization involving a Bayesian estimation.

The Bayesian estimation developed in Ref. 1 bears some similarities to the Richardson-Lucy deconvolution algorithm and involves the inversion of an integral relating the measured coherence of the acoustic field, the source distribution and the array response matrix.

1.5 Thesis Overview

The thesis is arranged into six chapters.

- **Chapter 1:** Introduces of topic of interest.
- **Chapter 2:** Provides a summary of the methodology that serves as the foundation for the present work.
- **Chapter 3:** Discusses the influence of the signal segmentation on the acoustic source maps.
- **Chapter 4:** Introduces and describes the experimental setup.
- **Chapter 5:** Presents and discusses the results.
- **Chapter 6:** Conclusion and recommendations for future work.

Chapter 2

Background

This chapter outlines the key relations in the direct spectral estimation of Ref. 1, which included fixed and continuously-scanning sensors.

2.1 Model for the acoustic field

The direct spectral estimation approach involves the modeling of the noise source distribution so that the difference between the measured and the modeled statistics of the acoustic field are minimized in a least square sense. The simplest model for the jet noise source comprises a distribution of uncorrelated monopoles along the jet axis, as sketched in Fig. 2.1. The greek letter ξ represents the source coordinate. The axis x_m represents the line along which the scanning sensor travels. This line is parallel to the ξ axis. We allow for directional sources and denote the source distribution by $q(\xi, \theta, t)$, with θ being the polar angle measured from location ξ.

Assuming spherical spreading in a quiescent medium with uniform speed of sound a, the pressure recorded by a scanning sensor m is

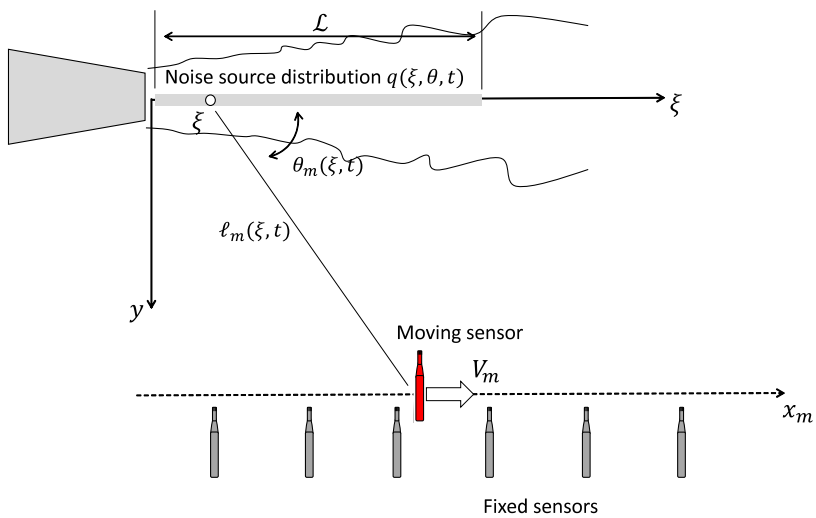

Figure 2.1: Schematic of a line source distribution

$$p_m(t) = \int_{\mathcal{L}} \frac{1}{\ell_m(\xi, t)} q(\xi, \theta_m(\xi, t), t - \tau_m(\xi, t)) d\xi \tag{2.1}$$

where

$$\tau_m(\xi, t) = \frac{\ell_m(\xi, t)}{a} \tag{2.2}$$

is the source-sensor propagation time and $\ell(\xi, t)$ is the source-sensor distance. The integration is limited to the region of interest, i.e. along the ξ axis where we expect significant noise sources. Computation of cross-spectra requires careful evaluation of the non-stationarity of the signals that is introduced by the scanning sensors (notice the time varying distance $\ell(\xi, t)$ and polar angle $\theta_m(\xi, t)$ on the above equation).

There exist several techniques to estimate the spectrum for a non-stationary signal. One of the most popular ones is the short-term periodogram.[28] It consists of dividing the signal into blocks and performing a short-time periodogram analysis. Downsides of this technique

include that the estimated time-varying spectra depend on the block size and that there is no significant guidance as to how to divide the signal for our application. A review of the different spectral estimation techniques identified the Wigner-Ville spectral estimator as one of the more robust ways to handle the correlation of non-stationary signals. It was thus adapted in the treatment of Ref. 29

Considering two random variables $u(t)$ and $v(t)$, the Wigner-Ville spectrum is defined as the Fourier Transform of the symmetric cross-correlation. The symmetric cross-correlation is

$$R_{uv}(t,\tau) = \left\langle u(t+\frac{\tau}{2})v^*(t-\frac{\tau}{2})\right\rangle \tag{2.3}$$

where $\langle\rangle$ represents the expected value (ensemble average) and $()^*$ is the complex conjugate. The Wigner-Ville sprectrum is thus

$$G_{uv}(t,\omega) = \int_{-\infty}^{\infty} R_{uv}(t,\tau)e^{-i\omega\tau}d\tau \tag{2.4}$$

To deal with the non-stationarity introduced by the time-varying distance of Eq. 2.1 the signal is divided into K blocks, depicted in Fig. 2.2. The block size has to be such that the signal can be considered to be quasi-stationary for each block. The signal division is done so that the following block approximations are made

$$\begin{aligned}
\tau_m(\xi,t) &\approx \tau_{mk}(\xi) + \left(\frac{\partial\tau_m(\xi,t)}{\partial t}\right)_{t=t_k} \\
\ell_m(\xi,t) &\approx \ell_{mk}(\xi) \\
\theta_m(\xi,t) &\approx \theta_{mk}(\xi)
\end{aligned} \tag{2.5}$$

where the subscript k represents the block index and t_k is the center of the block.

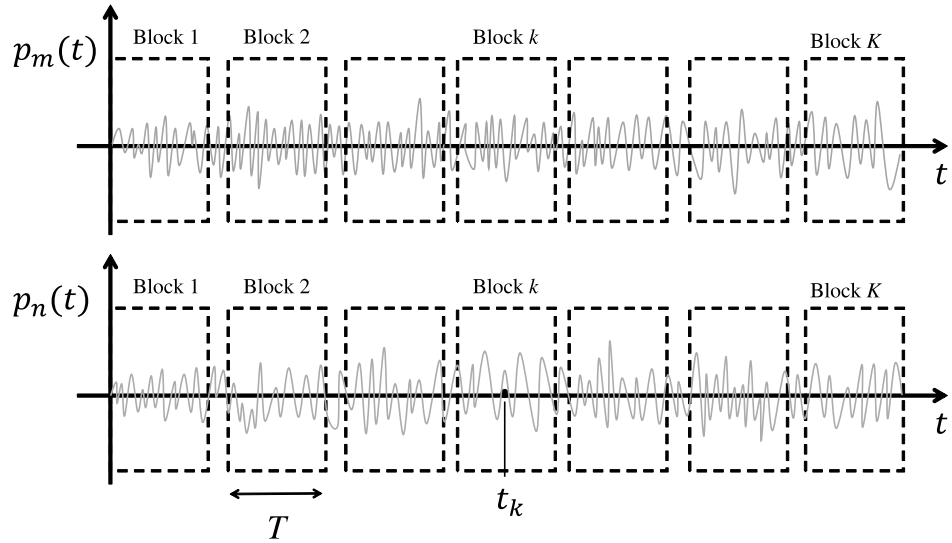

Figure 2.2: Segmentation of the pressure signal for sensors m and n into K blocks.

The equation for the pressure recorded by a scanning sensor m can be rewritten in terms of the block index k as

$$p_m(t) = \int_{\mathcal{L}} \frac{1}{\ell_{mk}} q(\xi, \theta_{mk}, \beta_{mk} t - \tau_{mk}) d\xi \tag{2.6}$$

where β_{mk} is a Doppler factor that stretches or compresses the time t. This parameter is directly related to the velocity of the sensor and its position and can be expressed as

$$\beta_{mk} = 1 - \left(\frac{\partial \tau_m(\xi, t)}{\partial t}\right)_{t=t_k} = 1 - \frac{V_m}{a} \cos\theta_{mk}(\xi) \tag{2.7}$$

The estimation of the acoustic source distribution involves cross-correlating the signals from multiple microphones, scanning or not, and computing the cross Wigner-Ville spectrum. Assuming that sensor n is moving with a velocity V_n and that sensor m is moving with a velocity V_m, the cross Wigner-Ville spectrum for block k is

$$G_{mnk}(t,\omega) = \int_{-\infty}^{\infty}\int_{-\infty}^{\infty} \langle p_{mk}(t+\frac{\tau}{2})p_{nk}(t-\frac{\tau}{2})\rangle e^{i\omega\tau} d\omega \tag{2.8}$$

where the term enclosed by $\langle\rangle$ is the symmetric cross-correlation. Using equation 2.6, the symmetric cross-correlation is expressed in terms of the source as

$$\begin{aligned}&\langle p_{mk}(t+\frac{\tau}{2})p_{nk}(t-\frac{\tau}{2})\rangle = \\ &\int_{\mathcal{L}}\int_{\mathcal{L}} \langle q(\xi,\theta_{mk},\beta_{mk}(t+\frac{\tau}{2})-\tau_{mk})q^*(x,\theta_{nk},\beta_{nk}(t-\frac{\tau}{2})-\tau_{nk})\rangle dx d\xi\end{aligned} \tag{2.9}$$

The left hand side of the above equation is dependent on the time separation τ and weakly dependent on the time t (quasi-stationarity). The right hand side is stationary and should only depend on the time separation. Defining a new variable $t' = \beta_{nk}(t-\tau/2) - \tau_{nk}$, the equation can be rewritten as

$$\begin{aligned}&\langle p_{mk}(t+\frac{\tau}{2})p_{nk}(t-\frac{\tau}{2})\rangle = \\ &\int_{\mathcal{L}}\int_{\mathcal{L}} \langle q(\xi,\theta_{mk},t'+\tau')q^*(x,\theta_{nk},t')\rangle dx d\xi\end{aligned} \tag{2.10}$$

where $\tau' = t(\beta_{mk}-\beta_{nk}) + \frac{\tau}{2}(\beta_{mk}+\beta_{nk}) + \tau_{nk} - \tau_{mk}$ is a time separation that stretches or contracts with time t, causing the non-stationarity of the sensor correlation.

Defining the cross-spectral density of the source as

$$Q_{mnk}(x,\xi,\omega) = \int_{\infty}^{\infty} \langle q(\xi,\theta_{mk},t+\tau)q^*(x,\theta_{nk},t)\rangle e^{-i\omega\tau} d\tau \tag{2.11}$$

and combining Eqs. 2.8 and 2.9, we obtain an equation connecting the cross-spectral density of the source to the cross Wigner-Ville spectrum of the pressure signals

$$\begin{aligned} G_{mnk}(t,\omega) = \int_{\mathcal{L}}\int_{\mathcal{L}} \frac{2Q_{mnk}(x,\xi,\omega'_{mnk})}{\ell_{mk}(\xi)\ell_{nk}(x)[\beta_{mk}(\xi)+\beta_{nk}(x)]} \\ \times exp\Big(i\omega'_{mnk}[\tau_{nk}(x)-\tau_{mk}(\xi)]\Big) exp\Big(i\omega''_{mnk}t\Big) dx d\xi \end{aligned} \tag{2.12}$$

where ω'_{mnk} is a Doppler-shifted frequency and ω''_{mnk} is a frequency of oscillation due to the non-stationarity of the sensor correlation. The Doppler-shifted frequency is

$$\omega'_{mnk} = \omega \frac{2}{\beta_{mk}(\xi)+\beta_{nk}(x)} \approx \omega\Big[1+\frac{1}{2}\Big(\frac{V_m}{a}\cos\theta_{mk}(\xi)+\frac{V_n}{a}\cos\theta_{nk}(x)\Big)\Big] \tag{2.13}$$

The frequency of oscillation is related to the Doppler-shifted frequency as

$$\omega''_{mnk} = \omega'_{mnk}\Big(\beta_{mk}(\xi)-\beta_{nk}(x)\Big) \tag{2.14}$$

Using Eq. 2.7 this expression is further approximated as

$$\omega''_{mnk} \approx \omega\Big(\frac{V_n}{a}\cos\theta_{nk}(x)-\frac{V_m}{a}\cos\theta_{mk}(\xi)\Big) \tag{2.15}$$

Suppression of the non-stationarity in the cross-Wigner-Ville spectrum (the dependence on time t in the sensor correlations of Eq. 2.12), provided that only one microphone is scanning, implies that $\omega''_{mnk}\frac{T}{2} \ll 1$. This translates to

$$V_\mu T \ll \frac{\lambda}{\pi\cos\theta_{\mu k}} \tag{2.16}$$

where λ is the acoustic wavelength and the subscript μ indicates a generic scanning sensor. The equation establishes a relation between the acoustic wavelength that is being resolved, the velocity of the sensor and the block length in seconds. The condition can be reformulated as

$$V_\mu \delta = c_\lambda \lambda \tag{2.17}$$

where c_λ is the fraction of the acoustic wavelength that the sensor travels in time δ. Reference 1 presents more insight and the explicit formulation of the c_λ constant and how this condition is implemented in the spectral estimation algorithm.

For polar angles significantly greater or much less than 90°, the block time T should be selected such that the sensor travels a distance much smaller than the acoustic wavelength to be resolved. It can be shown that if the polar angle is close to 0°, the block length T is the minimum for a given sensor velocity. The constrain on the block length poses a challenge and is particularly meaningful at high frequencies where λ is small. At a reasonable sampling rate, the resulting block length may contain too few samples to accurately compute the auto- and cross-spectral densities. Furthermore, the block time cannot be selected based on the highest frequency to be resolved since it would compromise the results at lower frequencies where longer block times are acceptable. This naturally yields to a frequency-dependent windowing of the signal when the scanning sensors are involved, as depicted in Fig. 2.3.

The frequency-dependent windowing, or time localization, involves the multiplication of the signal within each block by a window $g(t, \omega)$ that satisfies the energy preservation

$$\int_{\frac{-T}{2}}^{\frac{T}{2}} |g(t, \omega)|^2 dt = T \tag{2.18}$$

.

As in Ref. 1, a Gaussian window of the form

$$g(t,\omega) = A(\omega)\exp\Big(-\Big[\frac{t}{\delta(\omega)}\Big]^2\Big) \tag{2.19}$$

is selected, with $\delta(\omega)$ being a time scale that declines with the frequency (see Eq. 2.17), effectively reducing the block size and with the amplitude $A(\omega)$ defined as

$$A(\omega) = \Big(\frac{2}{\pi}\Big)^{1/4}\sqrt{\frac{T}{\delta(\omega)}\frac{1}{\mathrm{erf}(\frac{T}{\sqrt{2}\delta(\omega)})}} \tag{2.20}$$

Additional details on how the frequency-dependent window is implemented can be found in Ref. 1.

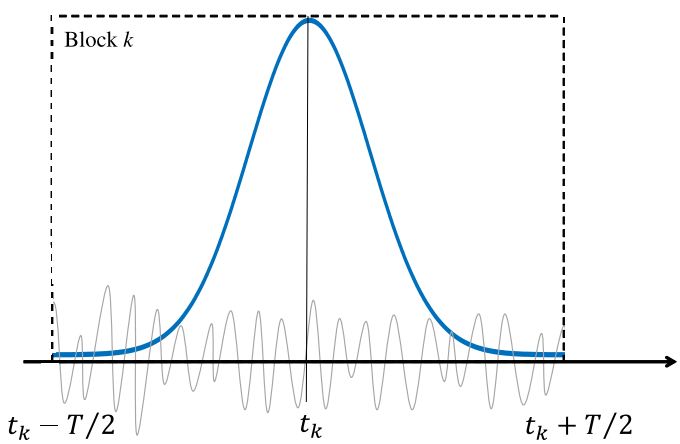

Figure 2.3: Example of the frequency-dependent windowing of the signal within a given block at a fixed frequency. The blue curve represents the Gaussian envelope $g(t,\omega)$ while the grey curve represents a random signal.

Having addressed the issues of the non-stationarity, Eq. 2.12 is approximated as

$$G_{mnk}(\omega) = \int_{\mathcal{L}}\int_{\mathcal{L}} \frac{Q_{mnk}(x,\xi,\omega'_{mnk})}{\ell_{mk}(\xi)\ell_{nk}(x)}\exp\Big[i\omega'_{mnk}\Big(\tau_{nk}(x)-\tau_{mk}(\xi)\Big)\Big]dxd\xi \tag{2.21}$$

It is further assumed that $G_{mnk}(\omega)$ can be estimated from the usual procedure

$$G_{mnk}(\omega) = \overline{P_{mk}(\omega)P^*_{nk}(\omega)} \tag{2.22}$$

where $P_{mk}(\omega)$ is the Fourier transform of $p_{mk}(t)$ and $\overline{()}$ indicates the averaging of PP^*. The Gaussian window is included in the spectral estimation algorithm.

Computation of the cross-spectral densities requires additional modeling of the source. Following the development in Papamoschou,[18] the source is modeled as

$$Q_{mnk}(x, \xi, \omega) = \psi(x, \omega)\Theta(x, \xi, \omega)\delta(x - \xi) \tag{2.23}$$

where $\psi(x, \omega)$ is the source distribution, $\Theta(x, \xi, \omega)$ is the directivity matrix and $\delta(x - \xi)$ is the Dirac delta. The directivity matrix is conveniently set to

$$Q_{mnk}(x, \xi, \omega) = \sqrt{G_{mmk}(\omega)G_{nnk}(\omega)}\ell_{mk}(\xi)\ell_{nk}(x) \tag{2.24}$$

Upon defining the complex coherence of the acoustic field as

$$\gamma_{mnk}(\omega) = \frac{G_{mnk}(\omega)}{\sqrt{G_{mmk}(\omega)G_{nnk}(\omega)}} \tag{2.25}$$

the equation for the acoustic source distribution in terms of the coherence of the acoustic field is

$$\gamma_{mnk}(\omega) = \int_{\mathcal{L}} e^{i\omega'_{mnk}(\tau_{nk}(x) - \tau_{mk}(x))}\psi(x, \omega)dx \tag{2.26}$$

It is convenient to introduce the array response matrix $Z_{mnk}(x_0, \omega)$ expressed as

$$Z_{mnk}(x_0, \omega) = e^{i\omega'_{mnk}\left(\tau_{nk}(x_0) - \tau_{mk}(x_0)\right)} \tag{2.27}$$

It describes the modeled coherence of the acoustic field for a point source located at x_0 with a frequency ω. Equation 2.26 is thus rewritten as

$$\gamma_{mnk}(\omega) = \int_{\mathcal{L}} Z_{mnk}(x, \omega)\psi(x, \omega)dx \tag{2.28}$$

2.2 Inversion Methods

This section provides additional background with respect to the inversion of the acoustic integral of Eq. 2.28. The section also summarizes the Bayesian estimation approach of Ref. 1. The reader is referred to the original source[1] for a detailed development of the Bayesian estimation approach.

The equation with the integral that relates the coherence of the acoustic field, array response matrix and the noise source distribution has to be inverted for all microphone combinations and for all blocks. The number of independent elements of the coherence matrix is depicted in Fig. 2.4, where M_f is the number of fixed sensors, M_s is the number of scanning sensors and K is the number of blocks. The number of independent elements of the coherence matrix can be inferred from the figure and is given by

$$J = M_f^2 - M_f + 1 + KM_s(M_s + 2M_f - 1) \tag{2.29}$$

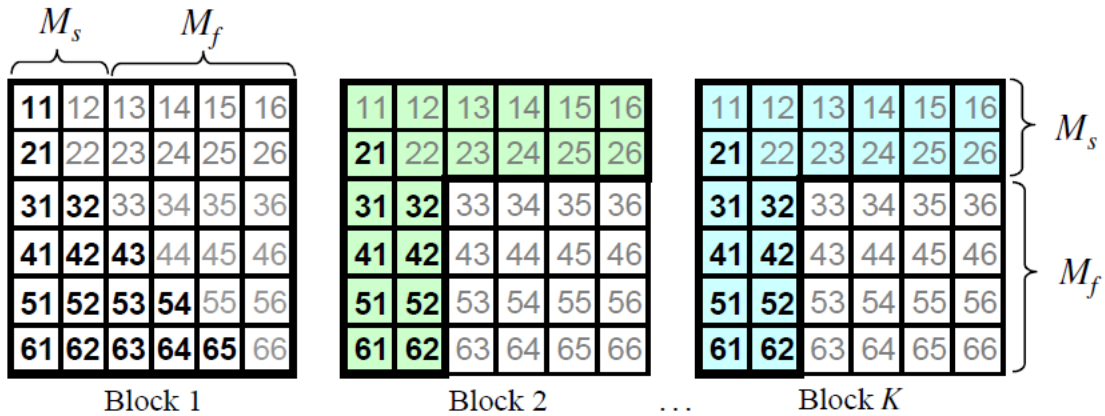

Figure 2.4: Illustration of the independent elements (bold) of the coherence matrices arising from $M_f = 4$ fixed sensors and $M_s = 2$ scanning sensors. Colored areas indicate the elements that vary from one block to the next. Off-diagonal elements comprise real and imaginary components. Diagonal elements are all equal to 1.

With that, Eq. 2.28 can be rewritten in terms of the number of independent elements as

$$\gamma_j(\omega) = \int_{\mathcal{L}} Z_j(x,\omega)\psi(x,\omega)dx \quad j = 1, ..., J \tag{2.30}$$

The previous equation can be approximated by writing the integral as a sum by dividing the region of interest into N_x uniform increments dx. The equation can be inverted by means of the Conjugate Gradient Minimization and by a Bayesian Estimation algorithm.

The conjugate gradient minimization is based on a least-square minimization and is done iteratively by using the restarted conjugate gradient method of Shanno and Phua.[25]

Typically, the region of interest is divided into smaller segments (N_x is between 200 and 500) to produce an accurate estimation. This causes the conjugate gradient method to be computationally expensive as it involves the calculation of the gradient in N_x directions for a number of function calls, and for each frequency. In general, 70 calls are enough to achieve convergence. If frequency vector contains 360 elements, and the region of interest is divided into 200 uniform segments, then the number of times that the gradient is calculated

is around 10^{160}. The method requires long run times when processing the entire range of a high-definition spectrum. On the other hand, it is feasible when examining a small number of frequencies (i.e. a narrow frequency range or coarse resolution of the frequency vector).

Due to the high computational cost of the conjugate gradient method, a Bayesian estimation approach was developed in Ref. 1. It bears similarities to the Richardson-Lucy deconvolution used in beamforming[30].[31] Considering a convolution integral of the type

$$\phi(\xi) = \int \psi(x) P(\xi, x) dx \tag{2.31}$$

Bayesian estimation seeks inversion by treating the variables involved (after the appropriate scaling when necessary) as probability density functions (pdfs); conditional pdf for $P(\xi, x)$ and total pdfs for $\psi(x)$ and $\phi(x)$. In traditional beamforming, $P(\xi, x)$ is the point spread function of the microphone array. While the integral of Eq. 2.28 seems like an unlikely candidate for this approach, it can be shown that it can be inverted with a Bayesian estimation algorithm. At fixed frequency, Eq. 2.30 takes the form

$$\gamma(\xi) = \int_{\mathcal{L}} \psi(x) Z(\xi, x) dx \tag{2.32}$$

Further difficulty arises from this equation when considering that both the coherence and the array-response matrix take values in the range from -1 to $+1$, while pdfs are supposed to be non-negative. This is overcome by using the self-consistency property mentioned by Papamoschou[18]

$$1 + \gamma(\xi) = \int_{\mathcal{L}} \psi(x)[1 + Z(\xi, x)] dx \tag{2.33}$$

The quantities $1+\gamma$ and $1+Z$ are non-negative, so the above integral now becomes a candidate for the Bayesian estimation approach. Its discrete version is

$$1+\gamma_j = \sum_{i=1}^{N_x} \psi_i (1+Zji) \tag{2.34}$$

The equation is inverted through the following iterative scheme

$$\psi^{(l+1)}(x) = \frac{\psi_i^{(l)}}{\sum_{j=1}^{J}(1+Z_{ji})} \sum_{j=1}^{J} \frac{(1+\gamma_j)(1+Z_{ji})}{\sum_{i=1}^{N} \psi_i^{(l)}(1+Z_{ji})} \tag{2.35}$$

where l denotes the iteration step. Typically, 2000 iterations are required to achieve convergence to an error (L_2 norm of the difference between the modeled and the measured coherence fields) of around 0.15. The Bayesian estimation algorithm gives results very similar to those calculated by the conjugate gradient minimization, and is at least an order of magnitude faster.

Chapter 3

Block distribution

The signal from the scanning sensor is non-stationary due to the time-varying source-sensor distance and polar angle. Quasi-stationarity is sought by dividing the signal into blocks. The block segmentation requires a careful evaluation of the block length and number of blocks. Criteria to determine the maximum and the minimum block size is provided in this chapter. A diagram showing the block size and number of blocks is presented as well, determining a safe region within which we consider the spectral estimations and the approximations on the statistics to be accurate. We only consider a uniform signal division, yielding to uniform-sized blocks.

3.1 Maximum block length

The segmentation of the signal into blocks is done so that a few approximations are made. The previous chapter presented an expression for the pressure recorded by a scanning sensor in terms of the block index k consisting of

$$p_m(t) = \int_{\mathcal{L}} \frac{1}{\ell_{mk}} q(\xi, \theta_{mk}, \beta_{mk} t - \tau_{mk}) d\xi \tag{3.1}$$

where m is the sensor index. This is depicted in Fig. 2.1. The above equation is only valid if the following approximations are true for each block

$$\begin{aligned} \tau_m(\xi, t) &\approx \tau_{mk}(\xi) + \Big(\frac{\partial \tau_m(\xi, t)}{\partial t}\Big)_{t=t_k} \\ \ell_m(\xi, t) &\approx \ell_{mk}(\xi) \\ \theta_m(\xi, t) &\approx \theta_{mk}(\xi) \end{aligned} \tag{3.2}$$

The maximum block size is thus directly determined from Eq. 3.2. The relation shows how the size of the block is connected to the array geometry; the maximum block size changes with the position of the scanning sensor.

Here, we propose a method to determine the maximum block length that involves the quantification of the error of the above approximations. To calculate the errors, the source-sensor distance is calculated at the center of the block and also computed at its downstream and upstream end. The polar angle and the source-sensor travel time are calculated at the same positions. These quantities are always determined with respect to a point situated at the edge of the nozzle.

The error of the source-sensor distance for each block is evaluated as

$$\begin{aligned} \epsilon_{\ell D} &= \Big|\frac{\ell_D - \ell_C}{\ell_C}\Big| \\ \epsilon_{\ell U} &= \Big|\frac{\ell_C - \ell_U}{\ell_C}\Big| \end{aligned} \tag{3.3}$$

where ϵ represents the error, the C, D, U are the center, downstream and upstream subscript, respectively and $|.|$ is the absolute value. Figure 3.1 illustrates the subscript convention. For reference, the source-sensor distance and polar angle are shown for the center of the block.

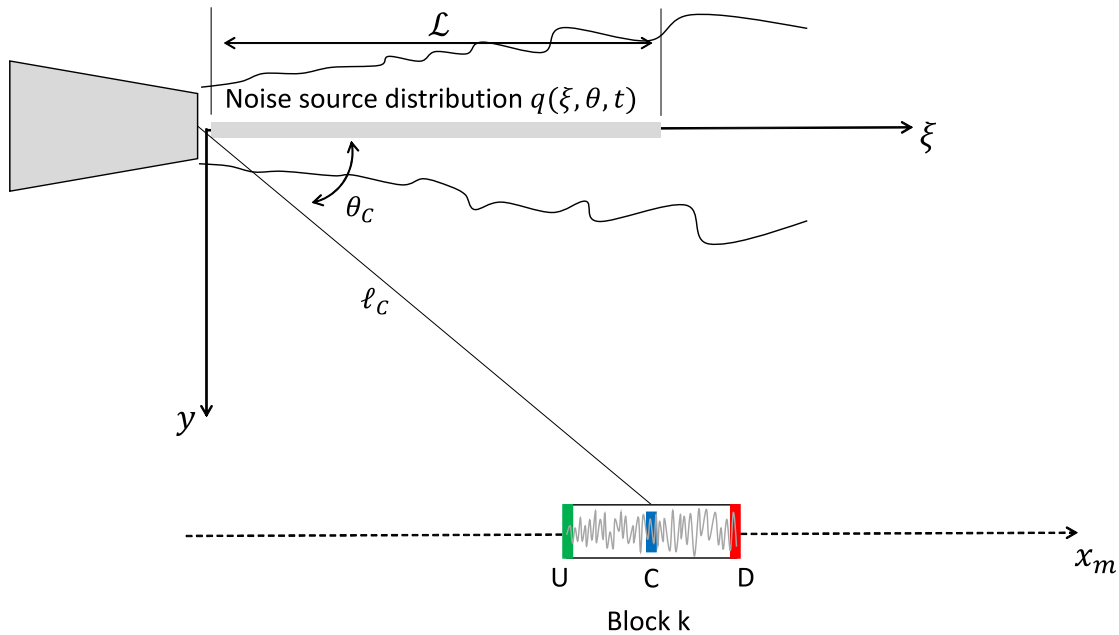

Figure 3.1: Subscript convention for the faces of the block. Letter U corresponds to the upstream facing end (marked in green), letter D corresponds to the downstream face (marked in red) and letter C corresponds to the center of the block (marked in blue).

These calculations are repeated to calculate the error of the polar angles

$$\begin{aligned} \epsilon_{\theta D} &= \left| \frac{\theta_C - \theta_D}{2\pi} \right| \\ \epsilon_{\theta U} &= \left| \frac{\theta_U - \theta_C}{2\pi} \right| \end{aligned} \tag{3.4}$$

The error on the source-sensor travel time is evaluated by comparing the difference between the first order Taylor expansion (see Eqs. 2.5 and 2.7) approximation on the faces of each

block and the actual value. The approximated source-sensor travel time at the upstream and downstream face of the block is

$$\begin{aligned} \tau_U &\approx \tau_{mk} - \frac{V_m}{a}\cos\theta_{mk}\frac{T}{2} \\ \tau_D &\approx \tau_{mk} + \frac{V_m}{a}\cos\theta_{mk}\frac{T}{2} \end{aligned} \tag{3.5}$$

Thus, the error between the approximation and the real value is

$$\begin{aligned} \epsilon_{\tau_U} &= \left|\frac{\tau_U - (\tau_{mk} - \frac{V_m}{a}\cos\theta_{mk}\frac{T}{2})}{\tau_U}\right| \\ \epsilon_{\tau_D} &= \left|\frac{\tau_D - (\tau_{mk} + \frac{V_m}{a}\cos\theta_{mk}\frac{T}{2})}{\tau_D}\right| \end{aligned} \tag{3.6}$$

where $\tau_U = \frac{\ell_U}{a}$ and $\tau_D = \frac{\ell_D}{a}$, and T is the length of the block in seconds.

The errors on the source-sensor distances, polar angles and travel times are calculated throughout the entire region covered by the scanning sensor, yielding to a high number of different block sizes. The size of each block is calculated with an iterative method, increasing the block size on every iteration, until the error of any of the parameters (polar angle, source-sensor distance or source-sensor travel time) is above a certain threshold. This threshold is typically set to be between 1% and 2%. To ensure the statistics are valid at all points, the maximum block size is selected as

$$N_{Bmax} = \min(N_B); \tag{3.7}$$

where min stands for the minimum, N_{Bmax} is the maximum number of samples of the block for the experiment and N_B are all the sizes calculated following the proposed method.

Due to our array geometry (depicted in Fig. 2.1), significant variations are typically expected at the position that is further downstream. In general, that point determines the maximum block size. Nevertheless, the above calculations are done for every position and for each experiment.

3.2 Minimum block length

The maximum block size is determined from the approximations of the statistics which involve the array geometry and the position of the scanning sensor. Opposite to that is the calculation of the minimum block size. The estimation of the minimum block length requires spectral considerations that require further scrutiny of the spectral estimation algorithm.

To visualize how the size of the Fourier Transform might affect the minimum block length, the basic steps involved in the spectral estimation are summarized. Consider a time signal $p(t)$ of duration T_T corresponding to one of the microphones. The signal is divided into K overlapping or non-overlapping blocks, each one of them containing N_B samples. Assuming a sampling rate of F_s, the block length in seconds is $T = N_B/F_s$. For the spectral estimation, each block is divided into S overlapping or non-overlapping segments. The segment overlap will be denoted by the greek letter σ and the size of the Fast Fourier Transform is denoted by N_{FFT}. The FFT algorithm requires that each segment contains $2N_{FFT}$ samples. The block length, the number of segments it contains and its overlap are related by the following equation

$$\sigma = \frac{2_{NFFT} - \frac{N_B - 2N_{NFFT}}{S-1}}{2N_{FFT}} \tag{3.8}$$

The above relation is further expanded to determine the block length as a function of the other variables yielding

$$N_B = 2N_{FFT}\big[(1-\sigma)(S-1)+1\big] \tag{3.9}$$

For a given size of the Fourier Transform and a fixed segment overlap, the minimum block length that is allowed is dependent on how many segments are required for a low variance spectral estimation. This is further expressed as

$$N_{Bmin} = 2N_{FFT}\big[(1-\sigma)(S_{min}-1)+1\big] \tag{3.10}$$

The variance of the spectral estimation needs to be evaluated to determine the minimum number of segments that are required. The method to evaluate the variance is summarized in the next lines. The algorithm starts with a block size described by Eq. 3.9 with $\sigma = 0.5$ and $S = 1$ for a given size of the Fourier Transform. The spectral estimation is done on the block and the Sound Pressure Level is calculated. Then the calculations are repeated with increasing by 1 the number of segments. The difference between the Sound Pressure Levels of consecutive segments is stored. The calculations are repeated for the number of segments pairs $S = 2, 3,\ S = 3, 4,\ ...,\ S = N, N+1$ where N is typically around 100. The number of segments selected is such that the difference between the Sound Pressure Level between consecutive segments is small and does not diverge. The difference of the Sound Pressure Level between segment pairs is plotted against the number of segments S and for different frequencies to assess the variance of the spectral estimation.

An example of the above process is presented in Fig. 3.2. The figure was obtained for the jet experiments shown in this work and using a size of the Fast Fourier Transform of 1024.

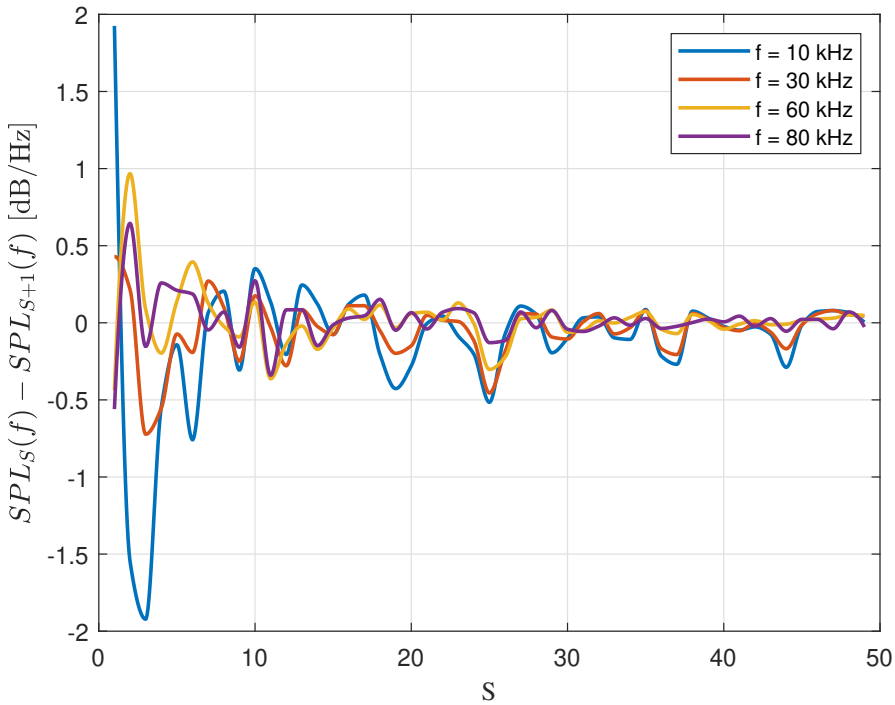

Figure 3.2: Sound Pressure Level difference between consecutive segment pairs.

The horizontal axis represents the number of segments and the vertical axis is the difference between the Sound Pressure Level computed with $S + 1$ segments and the Sound Pressure Level computed with S segments. It can be seen how the difference between the two reduces quickly to about $|0.4|$ dB/Hz and does not diverge.

The figure should be evaluated for each experiment as it is found to be subject to small variations. Typically, a number of segments greater than 10 is considered to be safe. The minimum number of segments will change depending on the source and the velocity of the scanning sensor.

3.3 Selection of the number of blocks

A range for the block length has been determined in the previous sections. This subsection studies the influence of the number of blocks and their overlap. It is clear that, for a fixed block length, a dense or a coarse signal segmentation might yield to high or low block overlap, respectively. The relation between the block overlap, the block size and the number of blocks is given by

$$K = \frac{\frac{N_B}{N_T} - 1}{\frac{N_B}{N_T}(\sigma - 1)} + 1 \tag{3.11}$$

where K is the number of blocks, N_T is the total number of samples of the signal and σ is the block overlap. The quantity N_B/N_T is the dimensionless block size.

A big block overlap yields to contiguous blocks containing essentially the same information with no clear advantage in terms of resolution or computation time. In such a case, it might be beneficial to merge these contiguous blocks into a new one with a bigger length. However, this can present a potential problem if the size of the block is close to the maximum size allowed, determined from Eq. 3.7. The opposite case is having blocks with little overlap. Low block overlapping can present a problem as the size of the block has to reduce to achieve it. If the size of the resulting blocks is smaller than the minimum size allowed, the accuracy of the spectral estimation is compromised. It is thus reasonable to determine a range of block overlapping that does not penalize the spectral estimation and avoids unnecessary computation time. Here, we set the range to be $\sigma = 0.1$ and $\sigma = 0.5$.

The combination of the results that limit the maximum and minimum block length and the number of blocks the signal is divided into is used to form an envelop containing a safe region. Within the safe region, we consider the spectral estimation and the pressure statistic approximations to be accurate. This is exemplified in Fig. 3.3. The horizontal axis

represents the dimensionless block length N_B/N_T, where N_T is the length of the signal, and the vertical axis represents the number of blocks. The bold lines are delimiting the envelope of the safe region. Line (a) establishes a relationship between the number of blocks and their dimensionless length for a 10% overlap. Line (b) is analogous to line (a) but for a 50% overlap. It is clearly shown how the safe region changes depending on the size of the Fast Fourier Transform. It also changes depending on the minimum number of segments considered for an accurate spectral estimation.

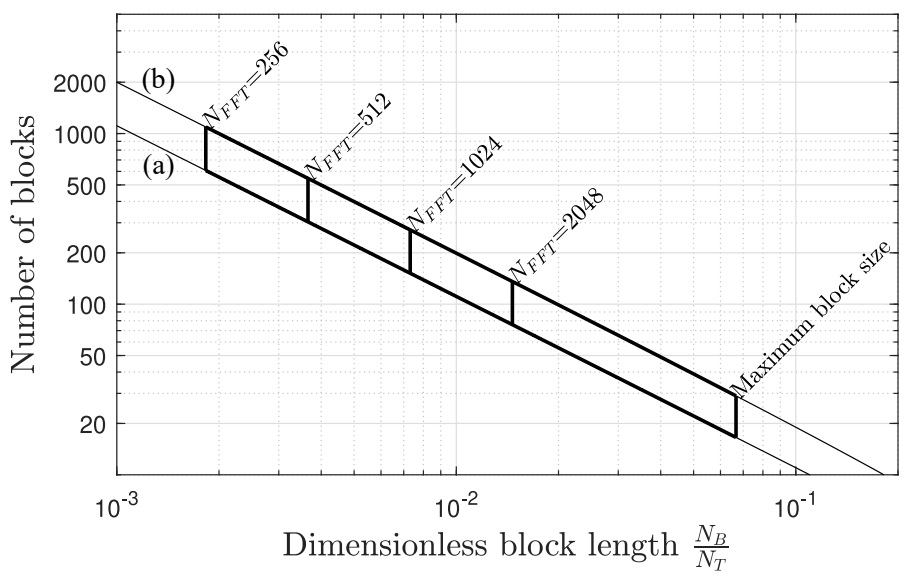

Figure 3.3: Example of the envelope showing the number of blocks versus the block length

The lines for the minimum sizes of the block of Fig. 3.3 are computed assuming that a total of 14 segments are necessary for an accurate spectral estimation (this is reasonable by examining Fig. 3.2). The maximum block size line has been obtained by setting the maximum allowed error on the approximations of Eq. 3.2 to 1%.

3.4 Width of the frequency-dependent window

The minimization of the frequency of oscillation in the cross-spectrum due to the non-stationarity of the sensor correlation motivated the implementation of a frequency-dependent windowing. The suppression of the non-stationarity, provided that only one microphone was scanning, implied that

$$V_\mu T \ll \frac{\lambda}{\pi \cos \theta_{\mu k}} \tag{3.12}$$

where V_μ is the velocity of the scanning sensor, T is the block length in seconds and λ is the acoustic wavelength that is being resolved. The equation suggested that, provided that the polar angle was significantly greater or less than 90°, the length of the block would have to shrink to solve the high frequencies. This condition was fulfilled by multiplying the signal within each block by a Gaussian window that satisfied the energy preservation and had the form

$$g(t, \omega) = A(\omega) \exp\Big(- \Big[\frac{t}{\delta(\omega)}\Big]^2 \Big) \tag{3.13}$$

with a time scale $\delta(\omega)$ that declined with frequency, effectively reducing the size of the block. The relationships for $\delta(\omega)$ and $A(\omega)$ correspond to Eqs. 2.17 and 2.20, respectively.

The size of the block is strongly connected to the frequency-dependent window. The percentage of the block that is neglected due to the implementation of the window might become important when the size of the block is not adequate for the frequency that is being resolved. This is particularly important when the high frequencies are resolved. The effective size of the block shrinks as the frequency increases due to the frequency-dependent window and the

information loss can be critical when resolving the high frequencies. This is exemplified in Fig. 3.4.

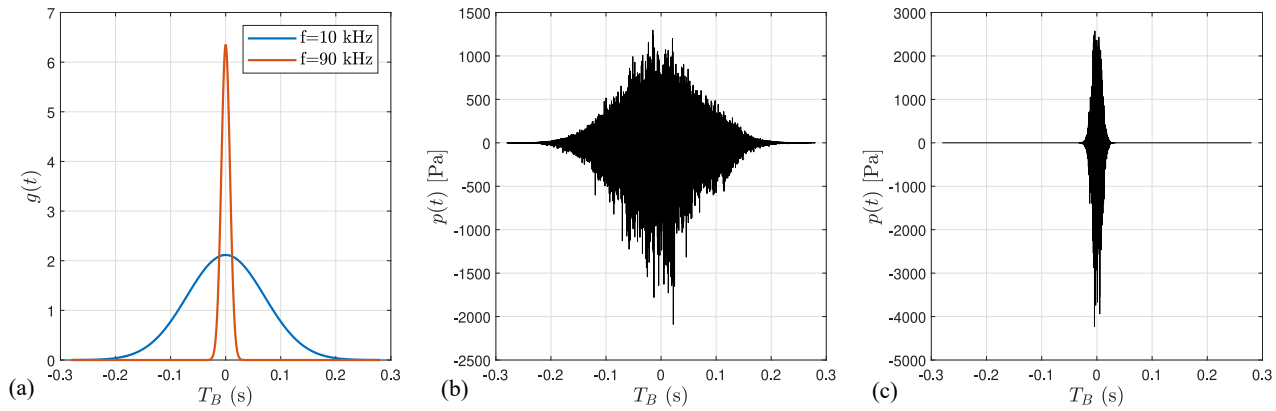

Figure 3.4: Example of frequency-dependent Gaussian window for two frequencies on a given pressure signal. (a) Shape of the Gaussian envelope; (b) Pressure signal multiplied by the Gaussian envelope for a frequency of 10 kHz; (c) Pressure signal multiplied by the Gaussian envelope for a frequency of 90 kHz;

Figure 3.4 has been obtained considering a block size that is close to the maximum allowed for a past experiment. The quantity T_B represents the size of the block in seconds, where $T_B = 0$ is the center of the block. The figure shows how very little information is used when computing the high frequencies if the block has a big size, causing the aforementioned information loss. To illustrate further how much information is neglected due to the implementation of the frequency-dependent window, the influence of the block size, number of blocks and the unused percentage of the signal is studied.

For convenience, we assume a block overlap of 50%. This means that we are situated on line (b) of Fig. 3.3. Using that, the size of the block and the number of blocks are related by Eq. 3.11 for $\sigma = 0.5$. The signal is considered to be neglected if the value of the Gaussian envelope is below 5% of its peak value. Figure 3.5 shows an example of the unused percentage of the block for different block sizes due to the frequency-dependent Gaussian window. The vertical axis represents the unused block size in percentage while the horizontal axis is the dimensionless block length. The vertical lines show the maximum size of the blocks and the

minimum size for different Fast Fourier Transform sizes. The color lines represent different frequencies.

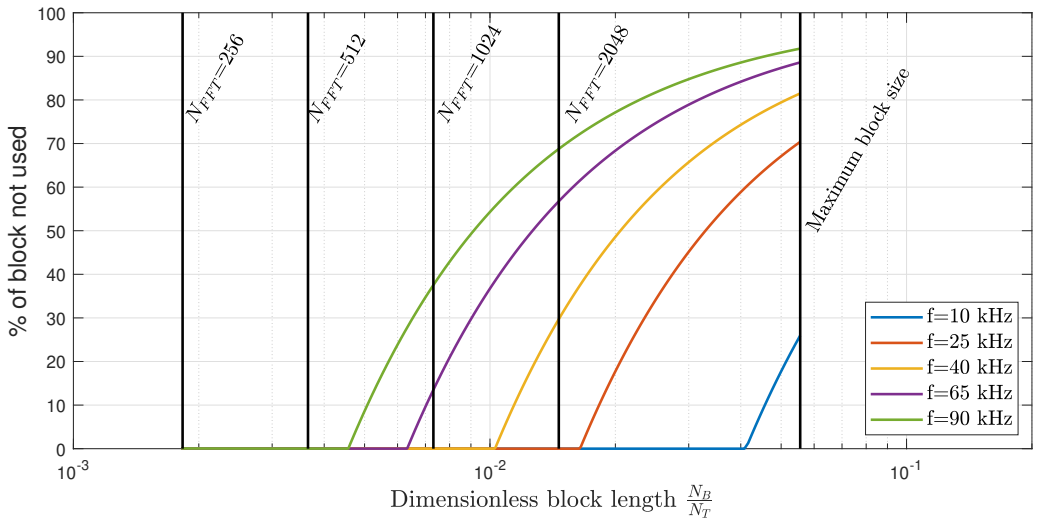

Figure 3.5: Example of the unused block size due to the effect of the frequency-dependent Gaussian window.

From the figure it is evident that there is a considerable information loss if the block size is not adequate. The figure also suggests that the percentage of the block that is not used is always higher when resolving the high frequencies if the size of the Fourier Transform is relatively big (for instance, $N_{FFT} = 1024$ and $N_{FFT} = 2048$). This motivates the use of different FFT sizes and block lengths accordingly to resolve the highest frequencies. A similar argument can be shown by combining Eqs. 3.9 and 3.12, obtaining

$$V_\mu(2N_{FFT})F_s\big(1-(\sigma-1)(S-1)\big) \ll \frac{\lambda}{\pi \cos_{\mu k}} \tag{3.14}$$

Realizing that $2N_{FFT}F_s$ is the length of the segment in seconds, the equation can be expressed as

$$V_\mu \Delta t_{seg} \ll \frac{\lambda}{\pi \cos_{\mu k}} \frac{1}{(1-(\sigma-1)(S-1))} \tag{3.15}$$

where Δt_{seg} is the length of the segments in seconds. Keeping the segment overlap and number of segments as constant, the equation clearly shows how the size of the segment needs to shorten as the frequency that is being resolved increases, implying that the size of the Fourier Transform needs to reduce as well.

3.5 Optimal block configurations

Upon determining the maximum and minimum block size, the effect of a dense or coarse signal division has been commented and related to the block overlap. A range for the block overlapping has been discussed. The suppression of the time-oscillation of the sensor cross-correlations yielded to the implementation of the frequency-dependent Gaussian window. The effects of the window have been evaluated in terms of the percentage of the block that is not used due to the shrinking of the window as a function of the frequency. To this extent, several comments have been made relating the block length, segment length and the size of the Fast Fourier Transform. All this information provides a few regions that we consider to be optimal where little information is lost due to the Gaussian window and where the spectral estimation is considered to be accurate. These regions are marked in green in Fig. 3.6.

The lines (a) and (b) are analogous to the ones shown previously in Fig. 3.3. The green region at the right hand side of the 2048 N_{FFT} line is considered to be optimal for that particular size of the Fourier Transform. However, the information lost when resolving the high frequencies is still considerable (see Fig. 3.5). Similarly for the region to the right hand side of the 1024 N_{FFT} line. Within this region, the information lost when resolving the

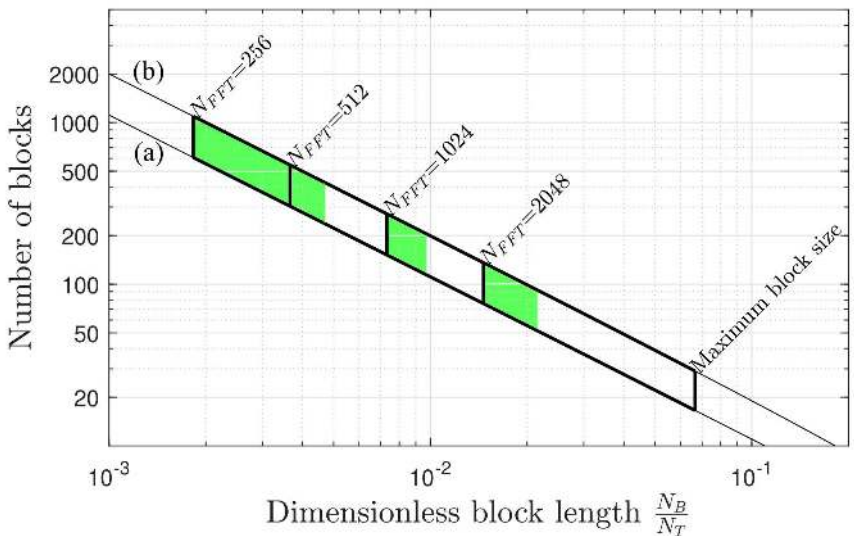

Figure 3.6: Example of the optimal regions as a function of block size and number of blocks.

high frequencies is less than in the previous case but there is still around 40% of the block that is not used when computing the highest frequency. The green region encompassing $N_{FFT} = 512$ and $N_{FFT} = 256$ does not have any gaps since the amount of information lost due to the frequency-dependent Gaussian window is relatively close to 0.

However, there exists a trade-off between the size of the Fast Fourier Transform and the frequency resolution and they are related as $\Delta f = F_s/N_{FFT}$ where Δf is the frequency resolution. As the size of the FFT increases, the frequency vector shortens and the number of frequencies resolved decreases accordingly.

A compromise solution is adopted when computing the noise source maps to take into account all the details that have been described previously. The noise source maps are created by patching several maps into one: each one of the maps has a different block size, size of the Fast Fourier Transform and distinct number of blocks. They all conserve the same block overlap. This is qualitatively sketched in Fig. 3.7.

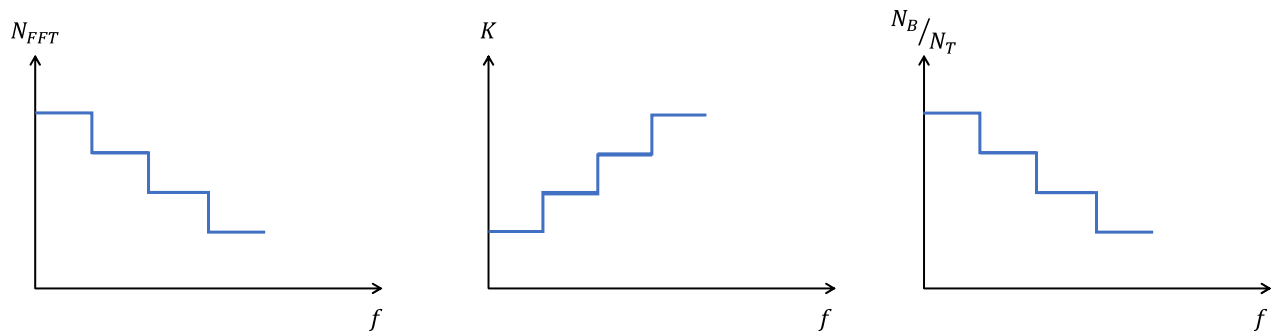

Figure 3.7: Sketch of the compromise solution that is adopted relating the size of the FFT, the number of blocks and the block length with the frequency.

In general terms, the safe region is always on the right side of the N_{FFT} lines depicted in Fig. 3.6. Typically, the closer they are to the FFT line, the less information is lost due to the frequency-dependent Gaussian window and we usually select points that are close to them

Chapter 4

Experimental setup

This section provides an overview of the experiments performed in the UCI aeroacoustics facility. Detailed information about the instruments used and the recording procedure is given. It also expands on the noise sources tested: an impinging jets source, that creates an approximation to a point source, and a supersonic jet supplied by a convergent-divergent nozzle that led to an overexpanded screeching jet. Finally, several block distributions are analyzed. Parts of this chapter are similar to or extracted from the AIAA Journal paper[1] as the experimental setup is the same.

4.1 Phased Microphone Array

All the noise measurements were conducted in the UCI aeroacoustics facility, depicted in Fig 4.1. The microphone phase array consists of up to twenty-four 1/8 inch condenser microphones (Brüel & Kjaer, Model 4138). These microphones are connected, in groups of four, to six conditioning amplifiers (Brüel & Kjaer, Model 2690-A-0S4). The outputs of the amplifiers are sampled simultaneously, at 250 kHz per channel, by three 8-channel

multi-function data acquisition boards (National Instruments PCI-6143) installed in a Dell Precision T7400 computer with a Xeon quad-core processor. National Instruments Labview software is used to acquire the signals with a custom build program and user interface.

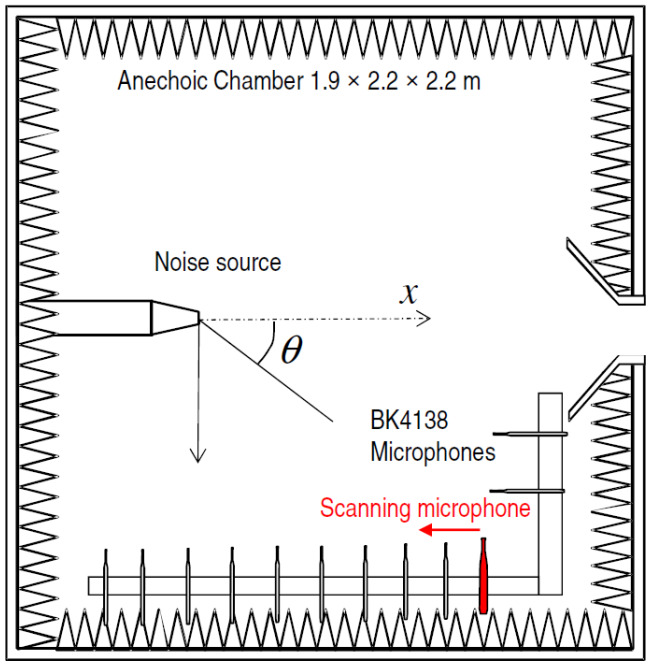

Figure 4.1: Anechoic chamber.

The 'atmospheric' details inside the anechoic chamber are measured: temperature and humidity are recorded to enable computation of acoustic atmospheric absorption and calculation of the exact speed of sound. The microphone signals are conditioned with a high-pass filter set at 350Hz to wipe out any possible DC noise signal. Narrowband sound pressure level (SPL) are typically computed using a 2048-point Fast Fourier Transform, yielding to a frequency resolution of 122Hz. The spectra are corrected for microphone actuator response, microphone free field response and atmospheric absorption, thus resulting in lossless spectra.

In this work, a total of 13 microphones are used, covering a polar sector from $\theta = 42°$ to $\theta = 73°$.

One continuous-scan microphone was mounted on a linear traverse consisting of a belt drive (Igus ZLW-0630) powered by a servo motor (ClearPath-MCPV). The design of the traverse system is depicted in Fig. 4.2. The path of the traverse was parallel to the line of the twelve fixed microphones that were mounted on the horizontal arm of the array holder (see Fig. 4.2). The scanning an fixed microphones had offset distances of 6mm, as illustrated in Fig. 4.3.

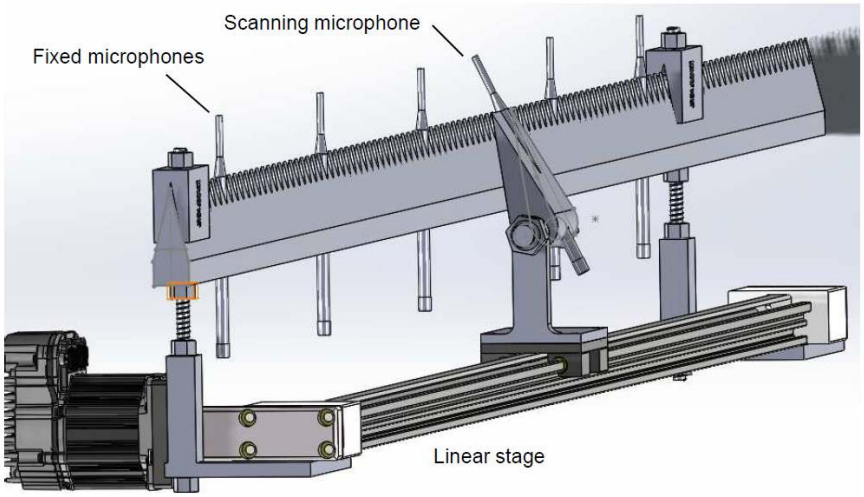

Figure 4.2: Design of the linear traverse system.

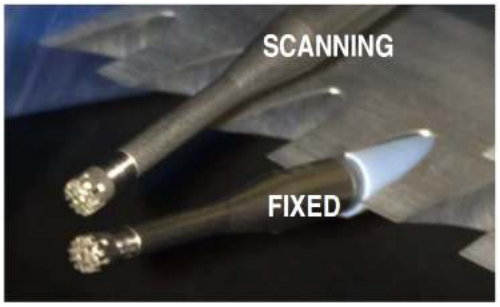

Figure 4.3: Fixed and scanning microphones at their closest spacing of 6mm, measured from the cartridge centers.

The servo motor was programmed to rotate at fixed RPM, moving the linear stage at a constant speed towards the source, with a total distance traveled of 580 mm and a speed of 69.13 mm/s. A total of 2100000 data points were acquired for each microphone data record.

Table 4.1: Summary of data acquisition parameters.

Number of scanning microphones	1
Number of fixed microphones	12
Sampling rate	250 kHz
Total samples	2100000
Linear scan speed	69.13 mm/s
Linear travel distance	580 mm
Acquisition time	8.4 s

The position of the moving microphone was known with an error within one millimeter, approximately. A summary of the data acquisition parameters is given in Table 4.1.

The coherence-based noise source maps presented in this work use all the array configurations and block distributions summarized in this section. A frequency-dependent Gaussian window with $c_\lambda = 0.2$ (Eq. 2.17) was used for all the noise source maps.

4.2 Determination of the Position of the Scanning Sensor

The position of the scanning sensor needs to be monitored and acquired in a way so that the microphone trace and the microphone signals are perfectly synchronized. The noise source localization is very sensitive to the location of the sensors and redundant systems have been implemented to guarantee an accurate reading of the position trace. A review of the signal synchronization and acquisition is presented in the next lines.

The signals from the microphones are sampled simultaneously, at 250 kHz, following the procedures mentioned in the previous section. In addition to the microphone traces, a synchronization and a position channel are also recorded simultaneously and sampled at the same frequency. The synchronization channel is constructed by splitting the voltage input of the ClearPath-MCPV into a channel connected to an SCB-68 card. This card is connected to a data acquisition board (National Instruments PCI-6143). The synchronization channels is also filtered at 350 Hz to remove any DC device noise.

The synchronization channel data is used to detect the activation instant of the ClearPath-MCPV. This is obtained by finding the peak value of the voltage of the recorded signal. The start sample of the microphone traces is chosen to be the activation instant of the scanning sensor. In that way, any small delay in controlling and acquiring the experimental setup is avoided. Figure 4.4 shows an example of a pressure signal and a synchronization signal. The synchronization channel shows the moment that the ClearPath is activated. The blue part of the pressure plot includes the data used to compute the noise source maps for a past experiment with a duration of 8.4 seconds. The data plotted in black is not used.

The position trace of the scanning sensor is acquired from two sources. The ClearPath MSPV software is used to record the time trace of the scanning sensor for each experiment. At the

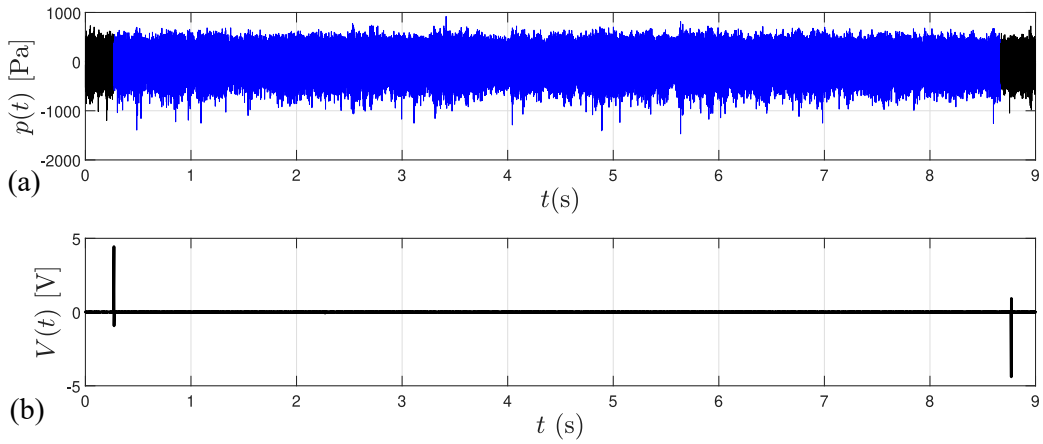

Figure 4.4: Example of the synchronization of the microphone traces with the position. (a) Pressure signal $p(t)$; (b) Synchronization signal

same time, secondary system also reads the position of the sensor. The system consists of a laser-based distance measurement device (SICK OD1000) that uses the triangulation principle to determine the position of a target. A point light is projected onto a small body attached to the scanning sensor and the distance is computed based on the angle of the reflected light, sketched in Fig. 4.5. The output voltage is proportional to the sensed distance and in the range of 0-10 V.

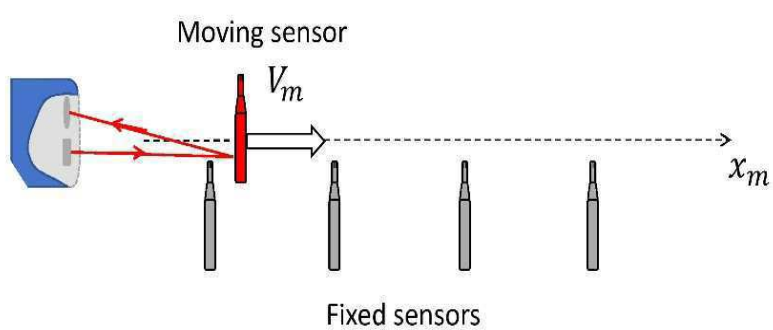

Figure 4.5: Laser-based distance measurement system.

The laser channel is connected to the SCB-68 card and is sampled simultaneously with the rest of the channels. However, the signal output from the laser sensor has to be conditioned to match the required input specifications of the PCI-6143. This is done by using a voltage

divider to map the original signal into a new one in the range of 0-5 Volts. A circuit diagram is shown in Fig. 4.6.

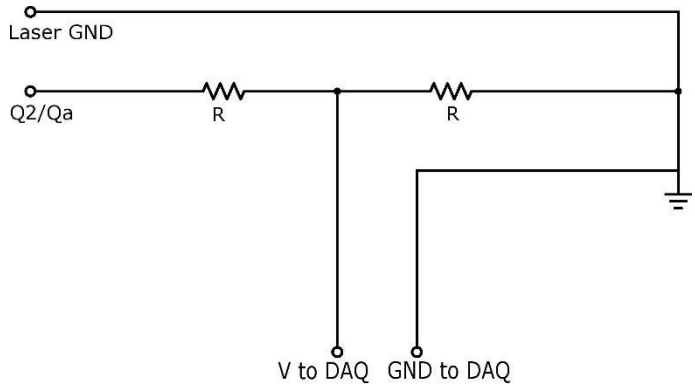

Figure 4.6: Voltage divider used to condition the signal output of the SICK laser-based displacement sensor.

The terminal $Q2/Qa$ represents the output of the SICK sensor and R represents a resistor. The abbreviation GND is used to refer to the ground terminal. The maximum voltmeter reading between terminals V to DAQ and GND to DAQ is never 5 V due to the dissipation of the circuit itself. In fact, the voltage reading between Q2/Qa and GND to DAQ is never 10 V either for the same reason. A calibration method is used so that the voltage reading is accurate and representative.

The position traces obtained with the ClearPath MSPV software and with the SICK OD1000 are compared after each experiment. An example is shown in Fig. 4.7.

The image on the left represents the complete scanned area while the image on the right is the error between the measurements taken with the Clearpath MSPV and the SICK laser-based distance measurement sensor. The reading from SICK is smoothed using a Savitzky-Golay filter. In addition, the signal from the laser is extrapolated when the scanning sensor reaches the maximum distance readable by the sensor. This distance is typically in the range of 0.6 to 0.7 meters.

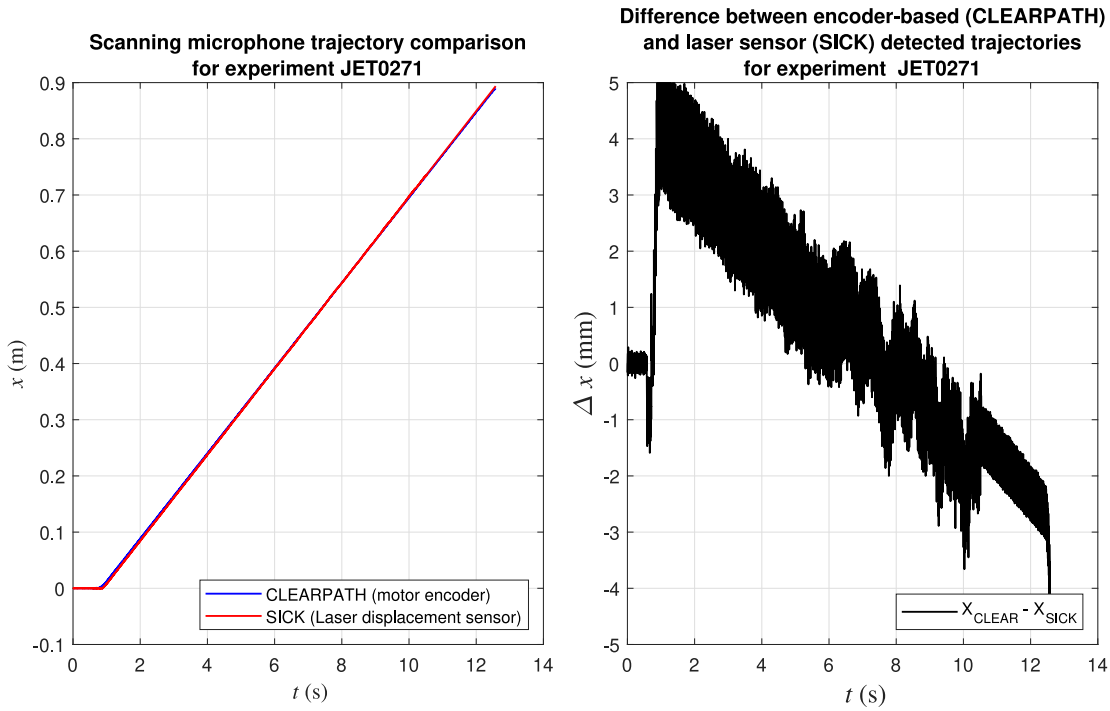

Figure 4.7: Scanning microphone trajectory comparison for experiment "JET0271".

4.3 Block distribution

A total of five block distributions are used to compute the noise source maps in this work. The signal processing developed in this work is compared to that done in previous publications (Ref. 1) to evaluate its performance. Thus, the configuration from the paper is named as "baseline configuration" and is summarized in Table 4.2. The noise source maps of this first configuration are constructed by patching the individual noise source maps computed with different sizes of the Fourier Transform that depend on the frequency. The patched noise source maps are constructed as follows: the results for a frequency up to 25 kHz are extracted from the noise source map with $N_{FFT} = 2048$. Then computations with $N_{FFT} = 1024$ are used for the frequencies between 25 and 50 kHz. The frequency range between 50 and 70 kHz uses the information of the noise source map with $N_{FFT} = 512$. Finally, noise source distribution for the highest frequencies is extracted from the acoustic source map computed

with $N_{FFT} = 256$. The block overlap is kept constant around 50% for all FFT sizes. Figure 3.5 is used to determine the frequency range for each block distribution.

Table 4.2: Summary of the different block distributions used in earlier work (Ref 1).

FFT size	Samples	Length (s)	Number of blocks	Overlap	Frequency Range (kHz)
2048	122880	0.492	35	52.68%	0-25
1024	122880	0.492	35	52.68%	25-50
512	122880	0.492	35	52.68%	50-70
256	122880	0.492	35	52.68%	70-90

The proposed signal segmentation yields to the computation of noise source maps with different FFT sizes and block sizes. A summary of the block distributions used to compute the patched noise source map is presented in Table 4.3. The map is obtained in a similar way as explained for the previous case except that the block sizes and number of blocks change depending of the size of the Fourier Transform and the frequency resolved.

Table 4.3: Summary of the different block distributions of the signal processing developed in this work.

FFT size	Samples	Length (s)	Number of blocks	Overlap	Frequency Range (kHz)
2048	36000	0.144	120	51.82%	0-25
1024	18000	0.072	242	52.00%	25-50
512	9656	0.039	436	50.23%	50-70
256	4578	0.018	919	50.14%	70-90

4.4 Array Configurations

The noise source maps presented in this work have been computed using different microphone array configurations and using various of block distributions. With regards to the array deployment, we use two different geometrical configurations: full and partial configuration, to display the benefits of the continuous-scan paradigm and to reveal the performance of a sparse microphone array with the proposed signal segmentation.

The array deployment configurations are depicted in Fig. 4.8, where the blue dots represent the position of the fixed sensors. The x axis is referenced to the jet nozzle exit and similarly for the y axis.

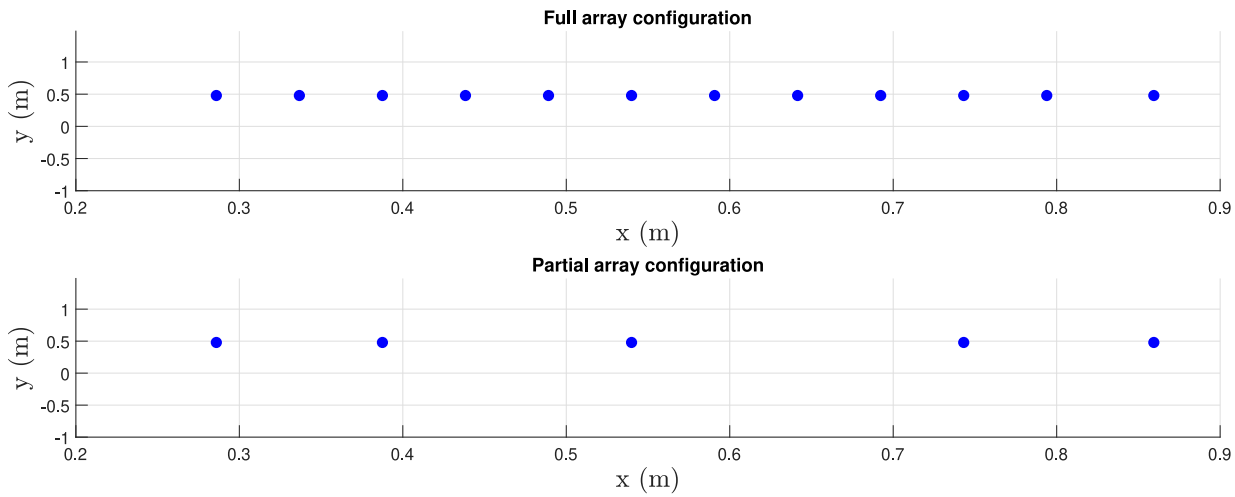

Figure 4.8: Array configurations showing the fixed sensors only. The figure on the top corresponds to the full array configuration (12 fixed sensors) while the image on the bottom is the partial array configuration (5 fixed sensors).

The full and partial microphone arrays that only use fixed sensors are denoted by F12 and F05, respectively.

The geometrical properties of the array configurations are investigated using a distance histogram. The distance histogram is a useful tool that enables a more complex visualization of the array geometry. In particular, it displays the distances between sensor pairs. When the scanning sensor is involved, the distance is calculated from the center of a block to the rest of the fixed sensors. The distance is as well calculated between fixed sensor pairs.

4.4.1 Full Array Configuration

The geometric deployment of the fixed and scanning sensors for the full microphone array using the base block configuration (Table 4.2) is depicted in Fig. 4.9. The scanning sensor is

shown at the block center times. The vertical axis represents the distance between the fixed and scanning sensor, choosing the y coordinate of the fixed sensors as the zero reference.

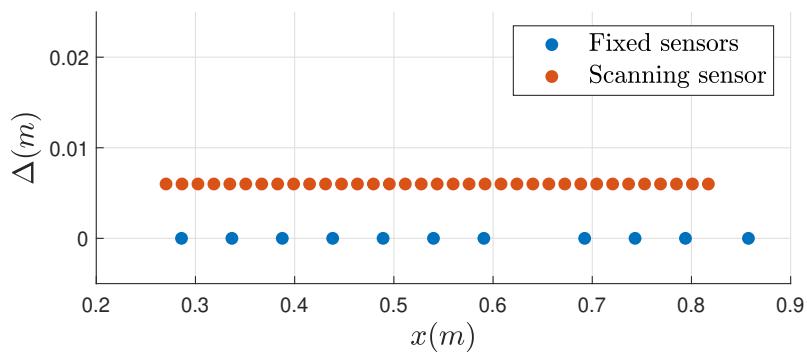

Figure 4.9: Full array with the base block configuration (35 block). Scanning sensor is shown at the block center times t_k.

The full array configuration that uses 11 fixed sensors and 1 scanning microphone is denoted by F11S01. The distance histogram for the base block configuration is presented in Fig. 4.10. It evidences how close the microphone pairs are to each other. The picture on the left is the complete distance histogram; the limit on the horizontal axis represents the maximum distance between microphones on the array. The picture on the right is a detail of the small distances.

The geometric deployment of the fixed and scanning sensors for the full microphone array using the other block configurations is not shown since there is a high number of points for the scanning sensor.

The histograms for the 120 and 242 block configurations are shown in Fig. 4.11 (a) and (b), respectively. The figure is constructed similarly to the previous one, showing the complete distance histogram and a detail of the small distances. A dense segmentation of the signal has a clear impact on the distance distribution between sensor pairs. The total number of distances that fall between the 0 and 10 mm range increases with increasing the number of blocks.

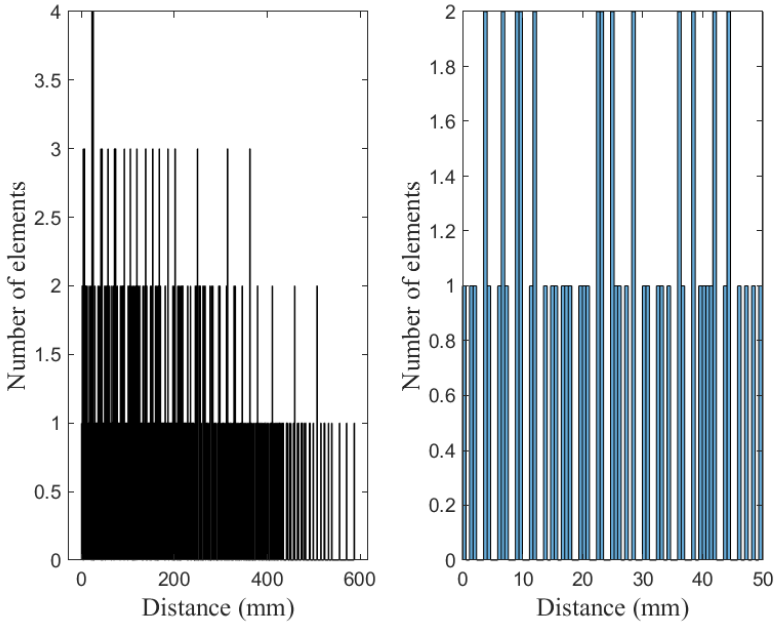

Figure 4.10: Distance histogram for the full microphone array using the 35 block configuration. The position at the block center time t_k is used when the scanning sensor is involved. The image on the left is the complete distance histogram. The image on the right shows a detail of the small distances of the histogram.

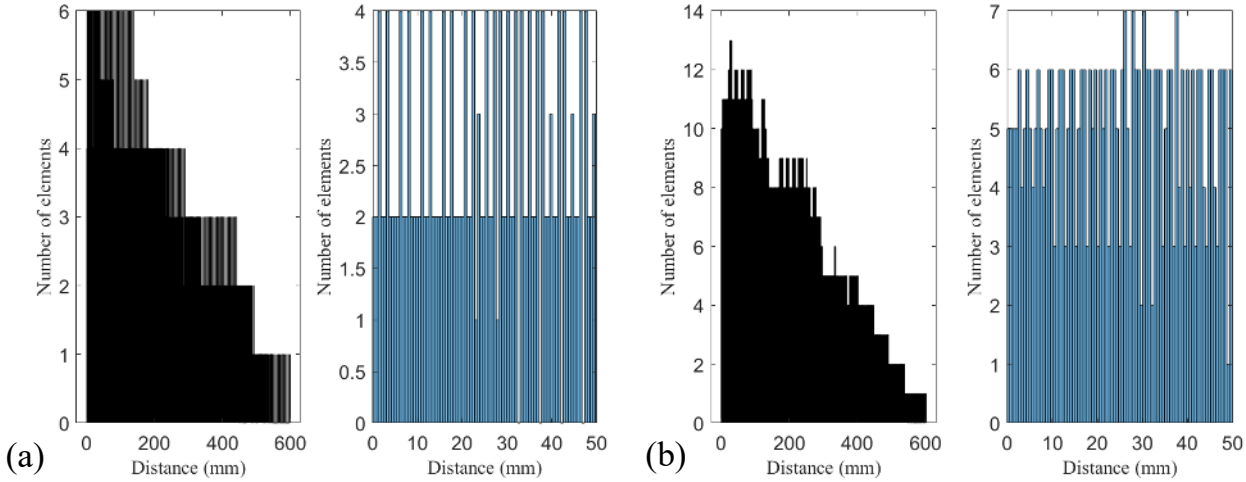

Figure 4.11: Distance histogram for the full microphone array using; (a) the 120 block configuration; (b) the 242 block configuration. For plots (a) and (b) the image on the left is the complete distance histogram. The image on the right shows a detail of the small distances of the histogram.

The histograms for the 436 and 949 block configurations are shown in Fig. 4.12 (a) and (b).

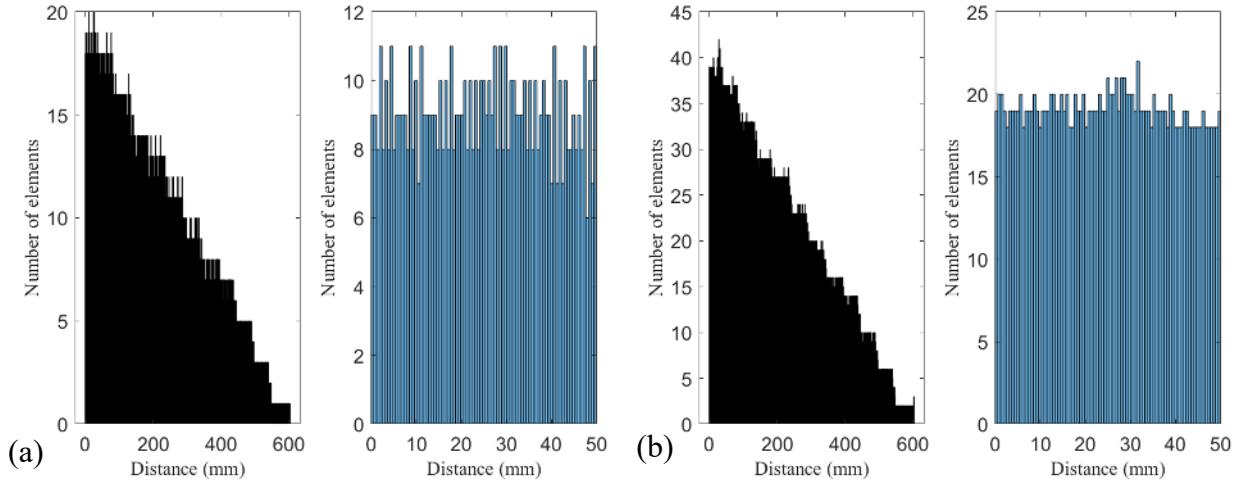

Figure 4.12: Distance histogram for the full microphone array using; (a) the 436 block configuration; (b) the 919 block configuration. For plots (a) and (b) the image on the left is the complete distance histogram. The image on the right shows a detail of the small distances of the histogram.

4.4.2 Partial Array Configuration

The array geometric deployment is also shown for the partial array configuration using the 35 block signal segmentation of Table 4.2. Analogous to the previous section, the scanning microphone is depicted at center times t_k in Fig. 4.13. The vertical axis represents the distance between the fixed and the scanning sensor with the zero reference chosen to be the fixed sensors.

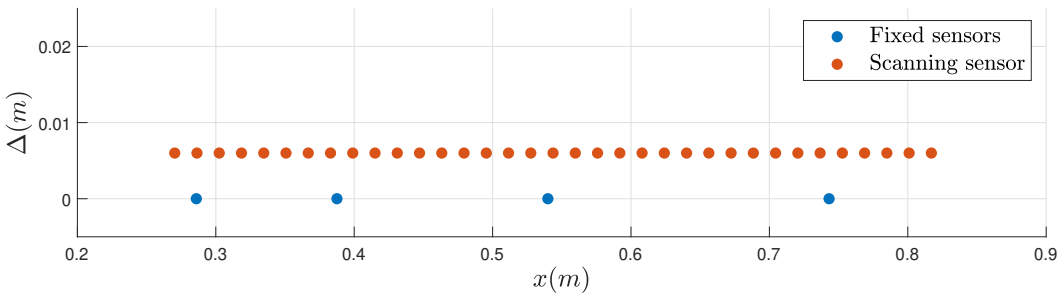

Figure 4.13: Full array with the base block configuration (35 block). Scanning sensor is shown at the block center times t_k.

The partial array configuration that uses 4 fixed sensors and 1 scanning microphone is denoted by F04S01. The distance histogram for the base block configuration (35 blocks) for the partial array is shown in Fig. 4.14. The figure shows clearly how the small distances are penalized for this particular block and array configuration, with just five microphone pairs between 0 and 10 mm.

The histograms for the 120 and 242 block configurations are shown in Fig. 4.11 (a) and (b), respectively. The effect of a dense segmentation of the signal has a stronger impact when using a sparse array configuration. In increases by a great factor the number distances of microphone pairs that fall between the 0 and 10 mm. A similar effect as earlier is seen: additional signal segmentation yields to an increased number of small distances between microphone pairs.

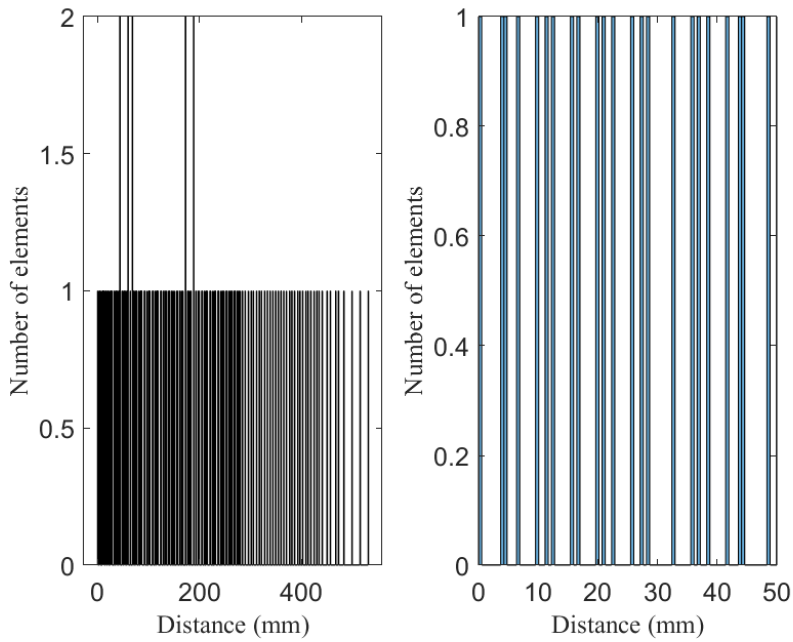

Figure 4.14: Distance histogram for the sparse microphone array using the 35 block configuration. The position at the block center time t_k is used when the scanning sensor is involved. The image on the left is the complete distance histogram. The image on the right shows a detail of the small distances of the histogram.

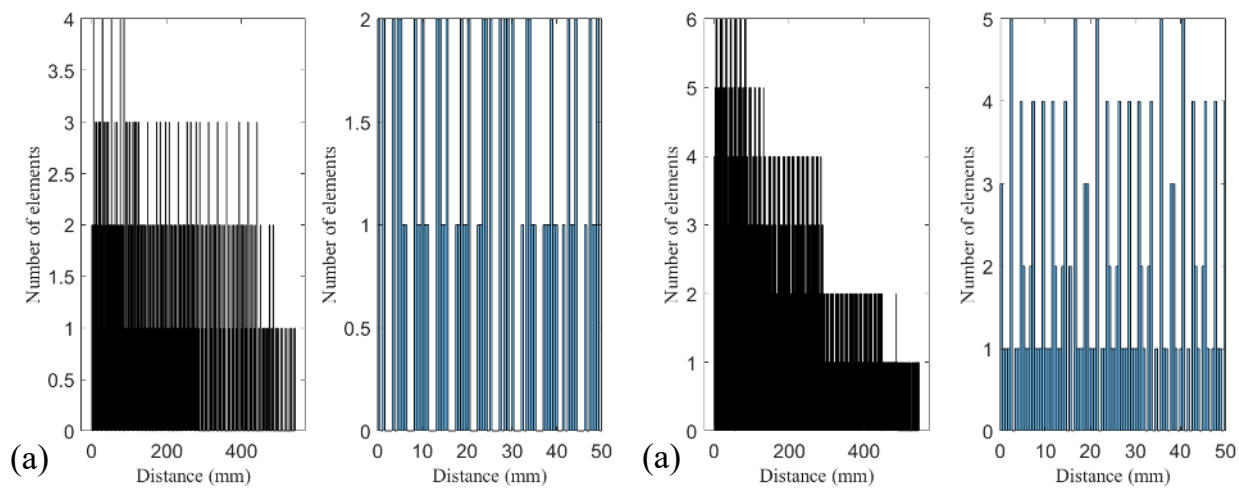

Figure 4.15: Distance histogram for the sparse microphone array using; (a) the 120 block configuration; (b) the 242 block configuration. For plots (a) and (b) the image on the left is the complete distance histogram. The image on the right shows a detail of the small distances of the histogram.

The histograms for the 436 and 949 block configurations are shown in Fig. 4.12 (a) and (b).

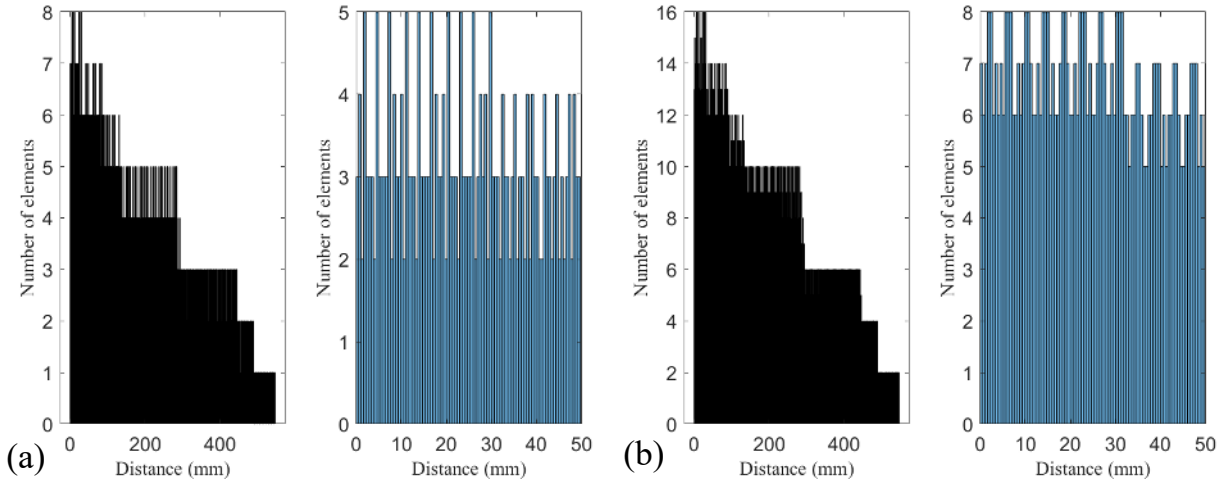

Figure 4.16: Distance histogram for the sparse microphone array using; (a) the 436 block configuration; (b) the 919 block configuration. For plots (a) and (b) the image on the left is the complete distance histogram. The image on the right shows a detail of the small distances of the histogram.

4.5 Noise Sources

Two very different acoustic sources were tested in this work. The first source was a supersonic jet that consisted of a convergent-divergent nozzle, designed by the method of characteristics for Mach 1.5 exit flow. The nozzle diameter was $D = 14.0$ mm. Figure 4.17 shows the radial coordinates of the nozzle and the plate.

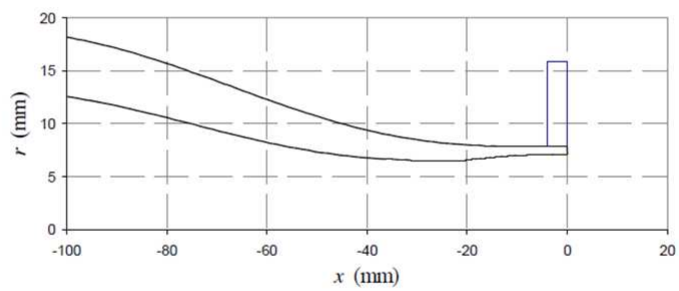

Figure 4.17: Radial coordinates of the nozzle and plate. The plate at the nozzle exit enhances the feedback mechanism loop.

The jet was supplied by cold air at a total pressure of 30 psig, resulting in an over-expanded exit condition with fully expanded Mach number of 1.38 and fully expanded exit velocity of $U = 403$ m/s. When the jet operates at such conditions, it emits strong broadband shock-associated noise in addition to turbulent mixing noise and screech. To accentuate the feedback loop involved with the screech, an annular flat plate of 30 mm diameter was attached to the nozzle exit.[6] A detailed image of the nozzle and the plate is shown on Fig 4.18. Although the detailed analysis of shock-associated noise was outside the purview of this study, this jet was selected because it contains random (broadband) and deterministic (tonal) sources, and is thus an interesting source field on which to test the imaging techniques.

The second source was an impinging-jets rig that bears a design similar to that used by Gerhold *et. al.*[32] It uses the collision of four jets to create an approximation to a point

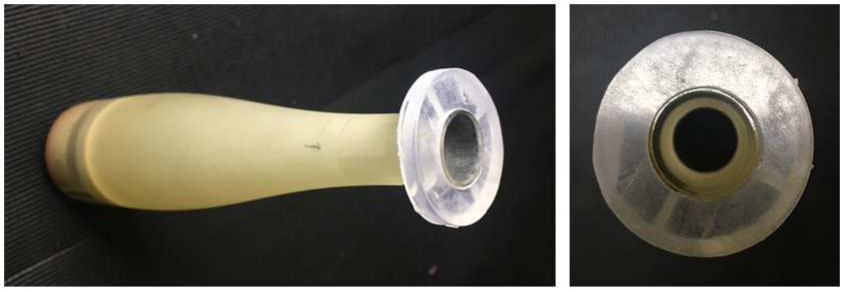

Figure 4.18: Image of the convergent-divergent nozzle with annular end plate.

source. The internal diameter of the tubes was 2.4 mm. The source was supplied by cold air at a supply pressure of 20 psig. The design is depicted in Fig 4.19.

Figure 4.19: Impinging jets source.

The support structures upstream of the source were covered with anechoic foam for both sources to avoid reflections and interference with the experiments.

4.6 Sound Pressure Level and Overall Sound Pressure Level

The data from the microphone signals at each surveyed polar angle is used to asses the directionality and the intensity of noise through the Sound Pressure Level (SPL) and the Overall Sound Pressure Level (OASPL). The fluctuation of the pressure signal $p(t)$ as a function of the frequency is determined using the power spectrum $S(f)$. The power spectrum of the pressure is the Fast Fourier Transform of the pressure fluctuation divided by a reference pressure p_{ref} (typically $p_{ref} = 20\ \mu$ Pa for air). It is thus computed as

$$S(f) = \mathcal{F}\left[\frac{p(t)}{p_{ref}}\right] \tag{4.1}$$

The raw sound pressure level (SPL_{raw}) uses the power spectrum $S(f)$ and transforms it to decibels per frequency (dB/Hz). It is defined as

$$SPL_{raw}(f) = 10 \log S(f) \tag{4.2}$$

The raw SPL has to be corrected for the atmospheric absorption of sound, the microphone frequency response and the free field response, resulting in a lossless spectra.

$$SPL(f) = SPL_{raw} + \text{corrections} \tag{4.3}$$

A very detailed description of how these corrections are done can be found in Ref. 33

The Overall Sound Pressure Level is used to assess the sound intensity for a particular polar station. It can be obtained by integrating the corrected Sound Pressure Level as

$$\text{OASPL} = 10 \log \int_0^{125\text{kHz}} 10^{0.1SPL(f)} df \tag{4.4}$$

Both SPL and OASPL plots are shown for the two sources used in this work.

Chapter 5

Results

This section summarizes the results obtained with the processing described in this work. The section is organized as follows: first the Sound Pressure Level and the Overall Sound Pressure Level are presented and discussed for the Impinging Jets Source and the overexpanded jet. The directivity of the sources as well as the peak emission is analyzed. Next, the acoustic source maps are presented for the Impinging Jets Source and then for the overexpanded jet. The maps are compared to those obtained in the previous work (Ref. 1) to evaluate the performance of the proposed signal processing.

5.1 Sound Pressure Level

5.1.1 Impinging Jets Source

Figure 5.1 shows the Overall Sound Pressure Level for the Impinging Jets Source measured the fixed sensors only. For this particular source we expect peak emission to be close to 90°. The emission is directive and the overall trend is to increase with the polar angle with the

exception of three polar stations. To view a which frequencies are dominating at which polar regions, we present the Sound Pressure Level.

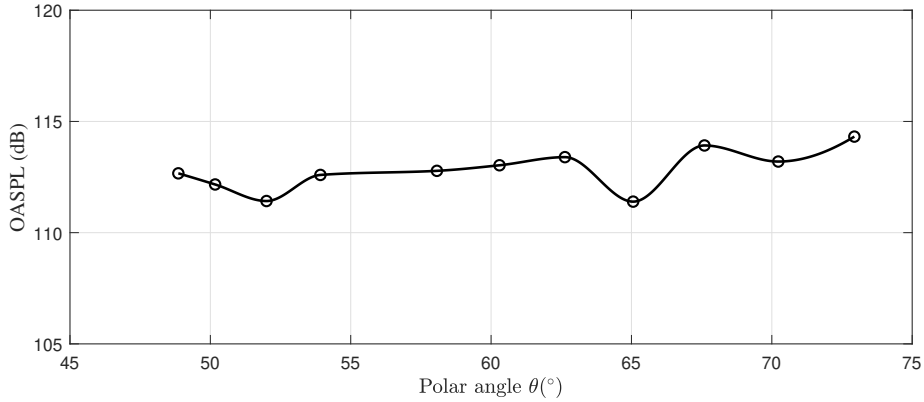

Figure 5.1: Overall Sound Pressure Level for the Impinging Jets Source.

The Sound Pressure Level of the source is shown in Figs. 5.2 and 5.3. The spectra are broadband and peak at a frequency of around 40 kHz.

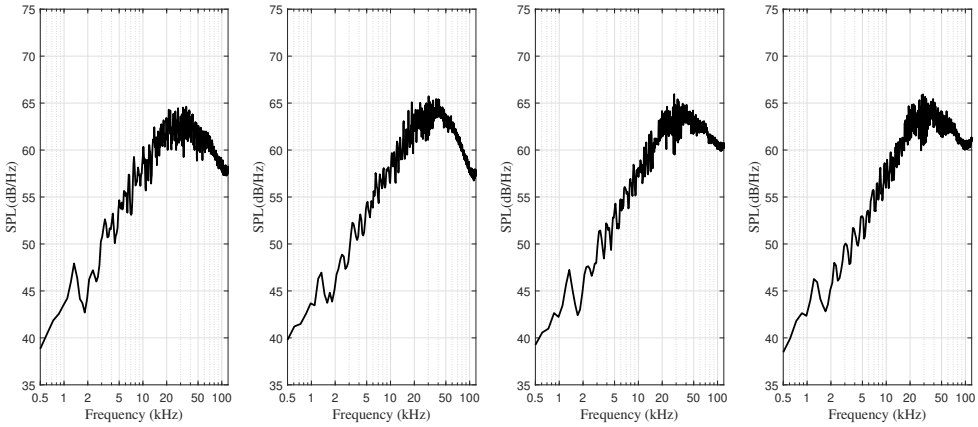

Figure 5.2: SPL spectra for the impinging jets source at different polar angles. The polar angles are, from left to right: $\theta = 48.2^\circ$; $\theta = 50.38^\circ$; $\theta = 54.17^\circ$; $\theta = 58.37^\circ$.

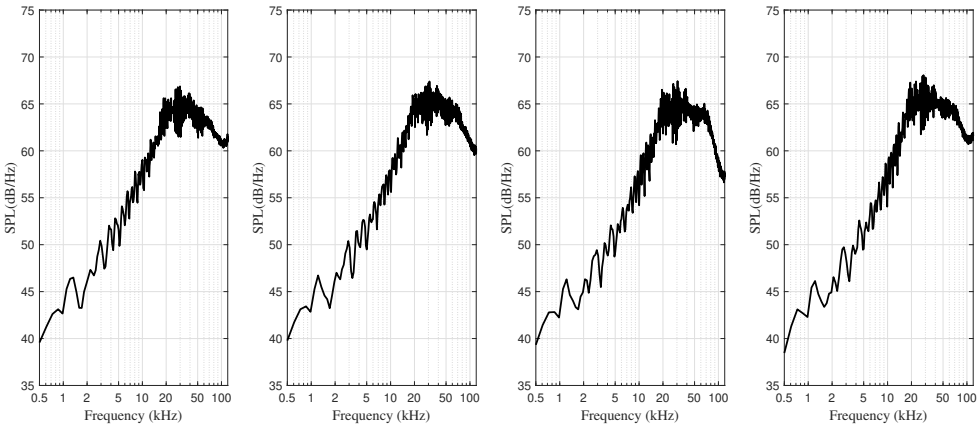

Figure 5.3: SPL spectra for the impinging jets source at different polar angles. The polar angles are, from left to right: $\theta = 62.98°$; $\theta = 68.00°$; $\theta = 70.65°$; $\theta = 73.40°$.

5.1.2 Overexpanded Jet

Figure 5.4 shows the Overall Sound Pressure Level for the Overexpanded jet measured using the fixed sensors only. The figure shows the directional nature of jet noise, with the OASPL undergoing significant variations with the polar angle. The OASPL peaks in the most downstream position as expected and its value reduces as the polar angle is increased.

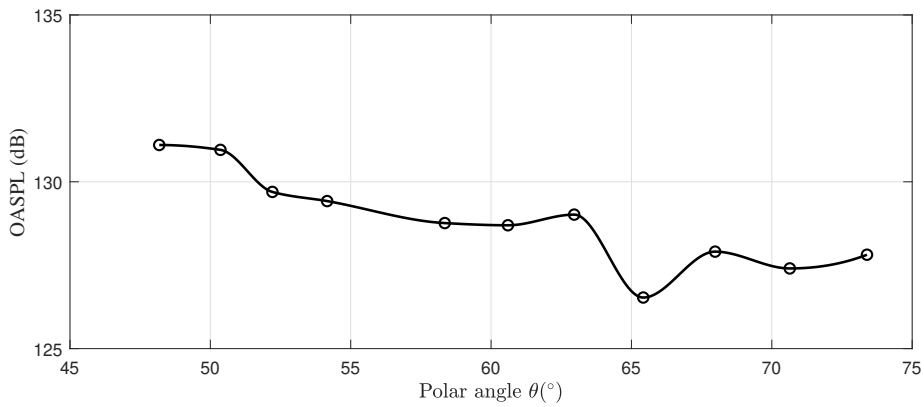

Figure 5.4: Overall Sound Pressure Level Overexpanded Jet.

Figures 5.5 and 5.6 show the Sound Pressure Level of the overexpanded jet at different polar angles. The screech tone near 10 kHz dominates most of the surveyed polar sector and is shown very prominently on both figures. At high polar angles, the harmonic near 20 kHz overtakes the base tone.

The jet exit velocity was, approximately, 403 m/s. With a jet diameter of 14.0 mm, the screech Strouhal number was $sr = fD/U = 0.35$, in line with the correlations found in Raman[6] for jets that have similar fully-expanded Mach numbers. The effects of the broadband shock-associated noise are clearly visible on Fig. 5.6, gaining prominence at high polar angles. The spectra is highly directional, with strong variations of the tonal noise as well as the shock-associated noise and the turbulent mixing noise.

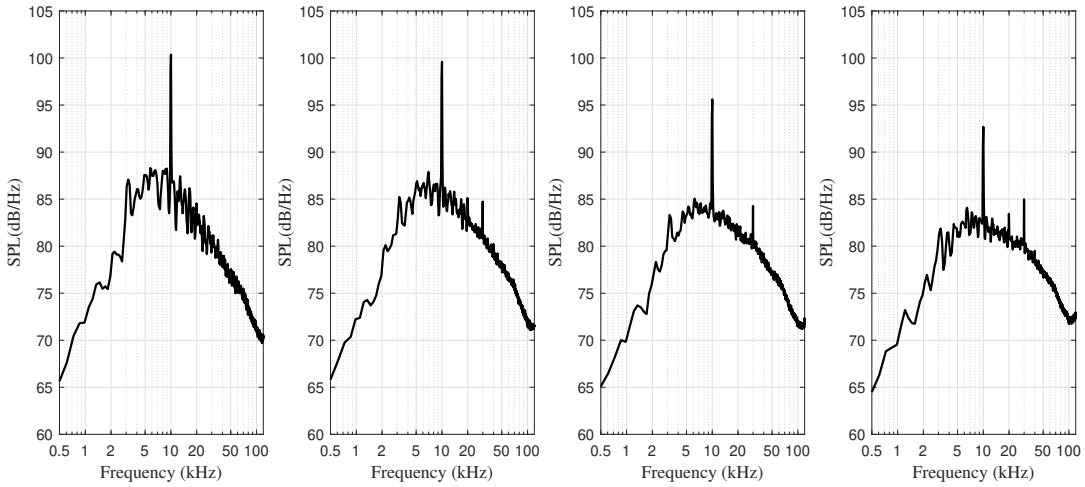

Figure 5.5: SPL spectra for the overexpanded jet at different polar angles. The polar angles are, from left to right: $\theta = 48.2°$; $\theta = 50.38°$; $\theta = 54.17°$; $\theta = 58.37°$.

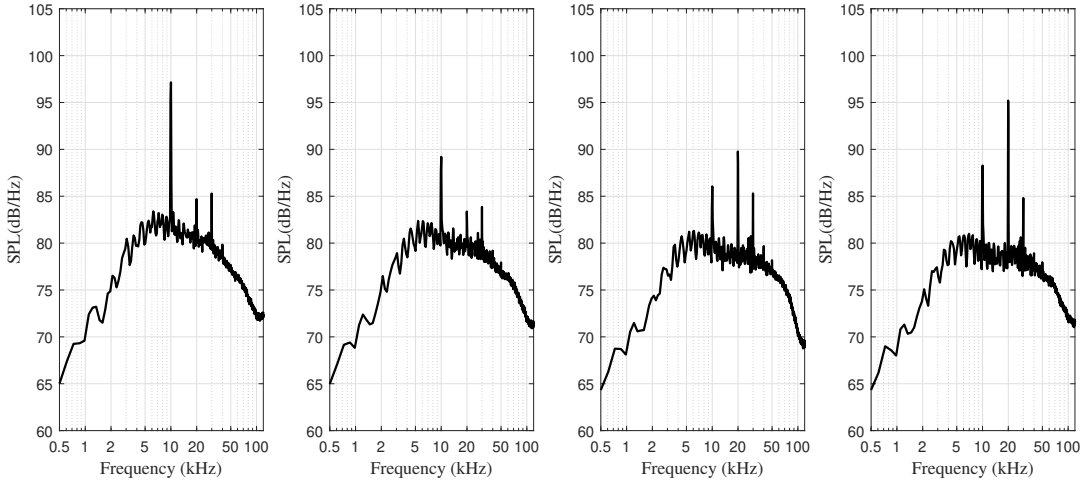

Figure 5.6: SPL spectra for the overexpanded jet at different polar angles. The polar angles are, from left to right: $\theta = 62.98°$; $\theta = 68.00°$; $\theta = 70.65°$; $\theta = 73.40°$.

5.2 Acoustic Source Maps

5.2.1 Impinging Jets Source

Figure 5.7 shows three coherence-based noise source maps for the full array configuration. The plots were obtained with the baseline block configuration (Table 4.2) when the scanning sensor was involved and the width of the frequency-dependent window used that $c_\lambda = 0.2$. The depicted acoustic source distributions were computed with different processing algorithms. The first (a) was obtained with the delay-and-sum method using the fixed sensors only (F12) while the second and the third were obtained by means of the Bayesian estimation method. Plot (b) only used the fixed sensors (F12) while 11 fixed sensors and 1 scanning microphone (F11S01) were used to compute plot (c).

The delay-and-sum noise source map suffers from clearly visible sidelobes and the source localization lacks of spatial resolution. Although it provides an approximate localization of the acoustic source, the fine spatial details are smeared out. The Bayesian estimation with F12 suppresses the sidelobes considerably and results in a more focused source at $x = 0$ m (the source becomes sharper compared to the delay-and-sum map). When the scanning sensor is involved (F11S01) the noise source map results in a highly localized source with almost imperceptible sidelobes. The displacement of the source towards positive values of x for the high frequencies is an artifact of the frequency-dependent patching.

Figure 5.14 shows two additional coherence-based noise source maps computed using the full array configuration and the Bayesian estimation method. Plots (a) and (b) correspond to F11S01 using the baseline block configuration and F11S01 using a block-patched noise source map, respectively (see Table 4.2). Both plots have been obtained by patching the results for different FFT sizes.

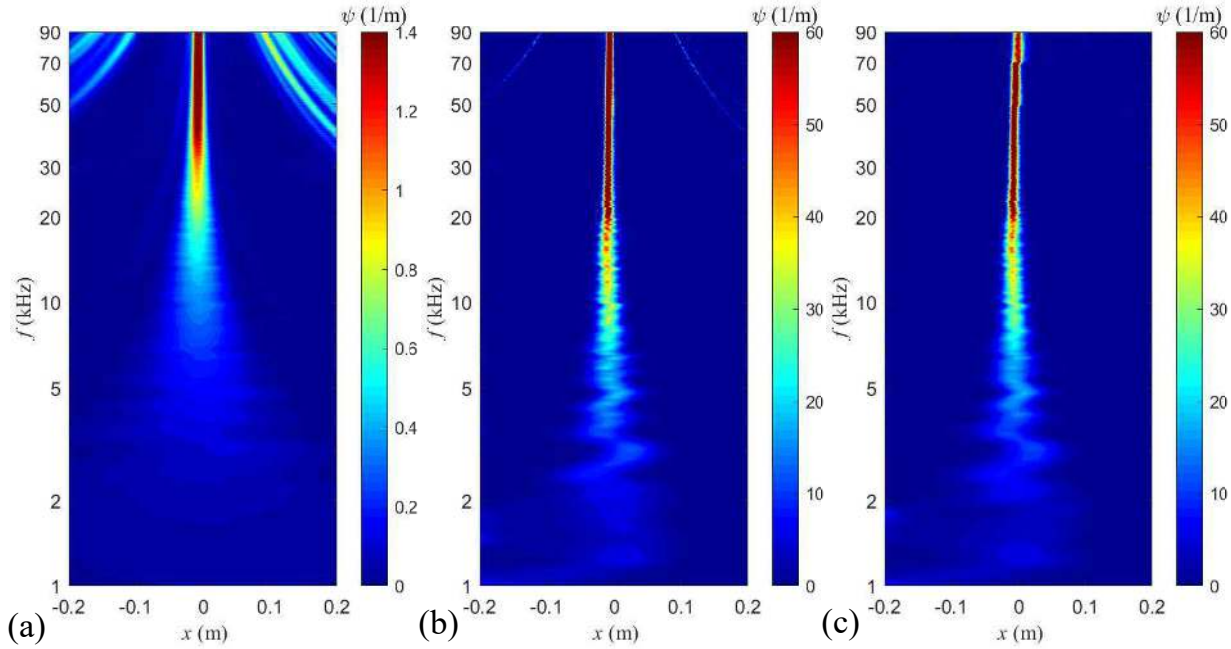

Figure 5.7: Coherence-based source strength $\psi(x, \omega)$ for the Impinging Jets Source using the full array configuration with the signal segmentation of Ref. 1. (a) Delay-and-sum (F12); (b) Bayesian estimation (F12); (c) Bayesian estimation (F11S01).

The image shows how the acoustic source becomes slightly sharper when using the block- and FFT-patched map. The proposed block segmentation yields to a cleaner source with a map that is practically devoid of sidelobes. The source small distance offset for the high frequencies is caused by the FFT-patching algorithm.

The performance of the proposed signal segmentation is also addressed by means of the distribution of distances between sensor pairs and the measured coherence of the acoustic field. With respect to the first, the distance histogram for the different block configurations is presented in Figs. 4.10, 4.11 and 4.12. It is seen how a dense block distribution such as the one used to compute the high frequencies has a high number of small distances between sensor pairs. This can be particularly useful depending on the coherence of the acoustic field.

The coherence assesses the similarity in the frequency domain between two signals. The measured coherence of the acoustic field between microphone pairs is plotted against distance.

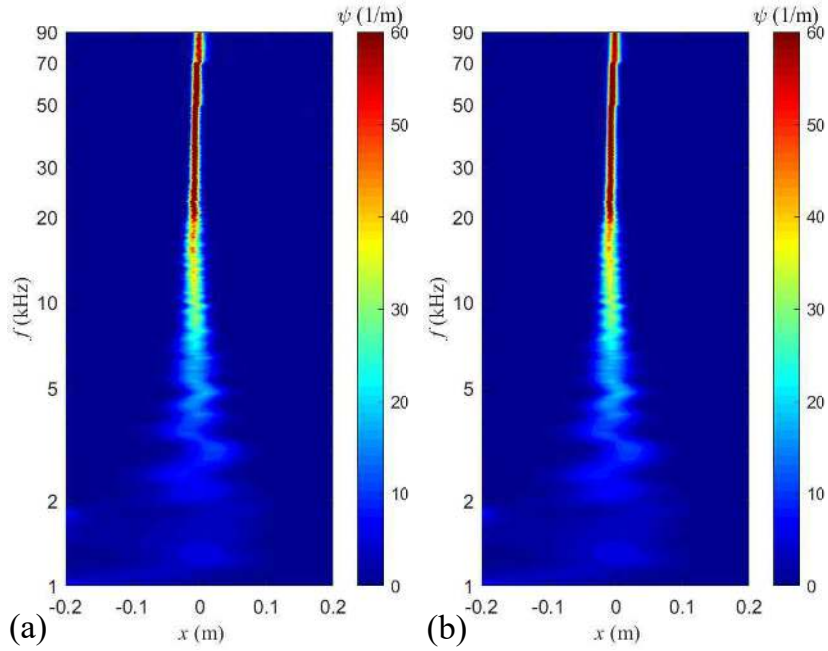

Figure 5.8: Coherence-based source strength $\psi(x, \omega)$ for the Impinging Jets Source using the full array configuration. (a) Bayesian estimation (F11S01) with the baseline block distribution of Ref. 1; (b) Bayesian estimation (F11S01) with the proposed block distribution.

This helps to visualize how far events with certain frequencies are related to each other and is used to determine a coherent envelope for each frequency. This is shown in Fig. 5.9. The vertical axis represents the absolute value of the measured coherence of the acoustic field γ for a particular frequency and between a sensor pair. The horizontal axis shows the distance between sensor pairs. The coherence of the acoustic field is computed as

$$\gamma_{mn}(\omega) = \frac{P_{mn}(\omega)}{\sqrt{P_{mm}(\omega)P_{nn}(\omega)}} \tag{5.1}$$

where P_{mm} and P_{nn} are the Fourier Transforms of $p_m(t)$ and $p_n(t)$, respectively, and $P_{mn} = \overline{P_{mm}P_{nn}}$ with $\overline{(.)}$ indicating the average.

The figure shows how all frequencies are coherent for relatively wide regions of space. This implies that, from the point of view of the source, having shorter blocks that are closer

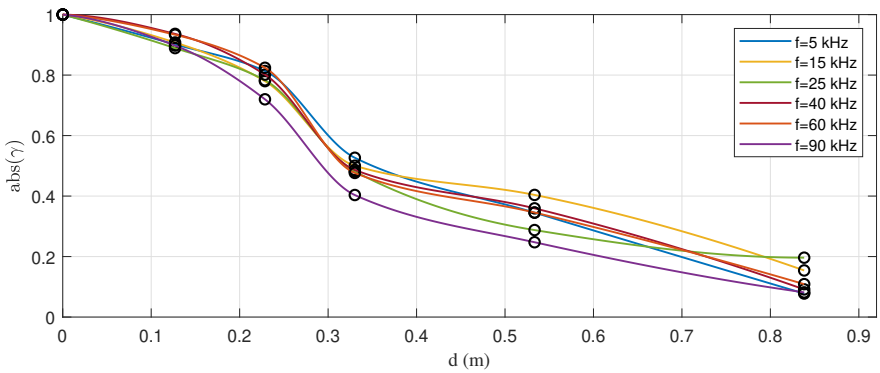

Figure 5.9: Measured coherence of the acoustic field for the Impinging Jets Source experiment as a function of the distance.

to each other will not necessarily benefit the resolution of the noise source map. Due to the nature of this acoustic source, less information is lost due to the frequency-dependent Gaussian window since the regions in which events are related to each other are relatively wide, allowing for a higher percentage of information loss. Thus this source allows bigger block sizes for similar reasons. This effect can be seen in Fig. 5.8; while the proposed signal segmentation -plot (b)- yields to a sharper source and a cleaner noise source map, the resolution of the high frequencies is comparable to that of plot (a), obtained with a fixed block size. However, it is predicted that the proposed block distribution should have a stronger impact on the high frequencies when using the partial array configuration, especially for the jet or sources with narrow spatial coherence on the far field.

Figures 5.10 and 5.11 are presented to illustrate the benefits of using a scanning sensor with a sparse array configuration. For these plots, a total of 5 microphones have been used.

Figure 5.10 shows three coherence-based noise source maps for the partial array configuration. The plots were obtained with the baseline block configuration when the scanning sensor was involved, in a similar way as before. The images (a), (b) and (c) were obtained similarly as those presented previously for the full array configuration. The delay-and-sum noise source map (a) is greatly dominated by the sidelobes. When using the partial array configuration,

the acoustic source on the DAS map blends with the sidelobes and it becomes difficult to distinguish any spatial features. The Bayesian estimation with fixed sensors (b) shows a clear improvement with respect to the delay-and-sum map. The level of the sidelobes is significantly reduced but on the other side, the source spatial resolution is very poor. The high frequencies are the most affected by the reduction in the number of microphones. Finally, the acoustic source distribution obtained with F04S01 (image c) is spatially well-resolved and there is no significant loss of the acoustic source distribution for the high frequencies. The sidelobes are minimal for this configuration. It is seen how the acoustic source map of F04S01 has a similar quality to that of F11S01, emphasizing the advantages of the continuous-scan paradigm.

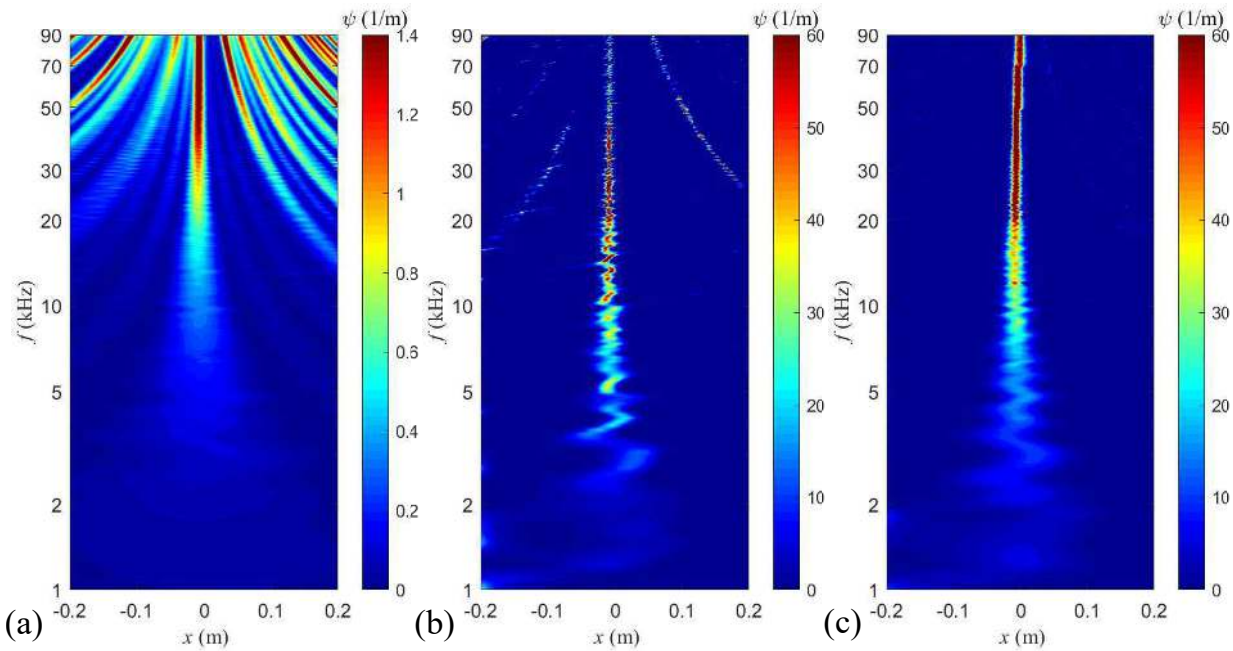

Figure 5.10: Coherence-based source strength $\psi(x, \omega)$ for the Impinging Jets Source using the partial array configuration with the signal segmentation of Ref. 1. (a) Delay-and-sum (F05); (b) Bayesian estimation (F05); (c) Bayesian estimation (F04S01).

Figure 5.11 illustrates the benefits of the newly proposed signal segmentation when using a sparse microphone array. Plots (a) and (b) correspond to F04S01 using the baseline block configuration and F04S01 using a block-patched noise source map, respectively (see Table

4.2). Both plots have been obtained by patching the results for different FFT sizes, similar as previously.

The figure depicts how the acoustic source becomes sharper when using the block- and FFT-patched solution. Both acoustic source images are practically devoid of sidelobes. It is worth noting that plot (b) has a similar quality to its equivalent computed with the full array configuration. The small distance offset of the source for the high frequencies is caused by the FFT-patching algorithm. Plot (b) seems to be cleaner than (a), indicating that the proposed signal segmentation is able to provide better spatially-resolved maps.

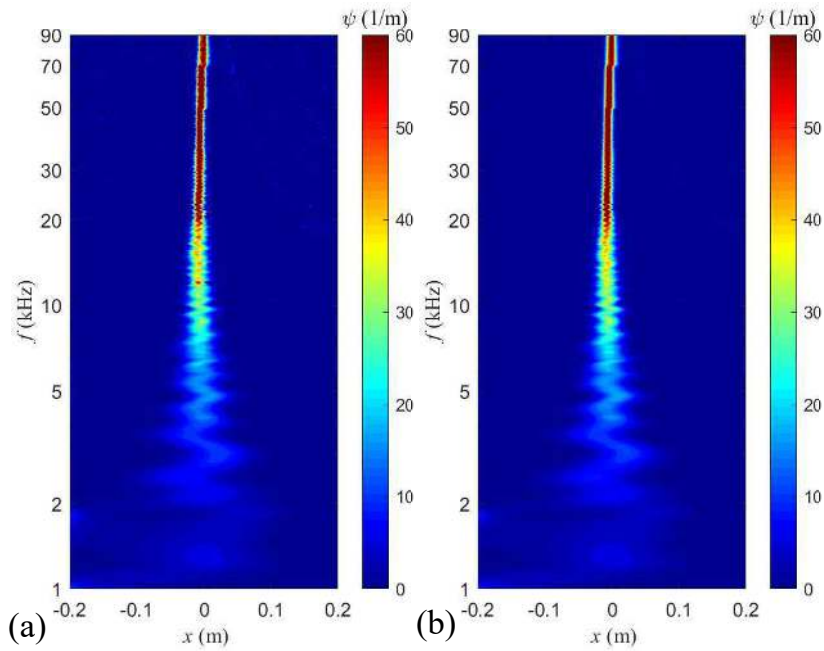

Figure 5.11: Coherence-based source strength $\psi(x, \omega)$ for the Impinging Jets Source using the full array configuration. (a) Bayesian estimation (F04S01) with the baseline block distribution of Ref. 1; (b) Bayesian estimation (F04S01) with the proposed block distribution.

This method is also applied to the overexpanded jet that presented the screech phenomena. The influence of a dense block distribution on the high frequencies can be further appreciated for that case, presented in the next section.

5.2.2 Overexpanded Jet

Figure 5.12 shows three coherence-based noise source maps for the full array configuration. The plots in this figure were obtained with the baseline block configuration (see Table 4.2) when the scanning sensor was involved. The fraction of the acoustic wavelength c_λ was set to 0.2 for all plots in this section. The noise source distributions in the figure were obtained with different algorithms, analogously to the Impinging Jets Source. Plot (a) was obtained with the delay-and-sum method while plots (b) and (c) were computed using the Bayesian estimation approach. Plots (a) and (b) used only fixed sensors (F12) and plot (c) used 11 fixed microphones and 1 scanning sensor (F11S01).

The delay-and-sum acoustic map is highly dominated by the sidelobes and it lacks of spatial resolution. The fine spatial details of the acoustic source are blurry and the source itself merges with the sidelobes, greatly affecting its spatial distribution at high frequencies. The reflection of the screech tone of a frequency of 10 kHz at the plate situated on the nozzle exit can be still be seen on the DAS source map. The Bayesian estimation with F12 (plot b) improves significantly the spatial resolution of the source to the point that the screech tone is better defined. However, the map is still influenced by clearly visible sidelobes. Finally, the Bayesian estimation with F11S01 suppresses considerably all the sidelobes and improves the spatial resolution of the Bayesian estimation with F12. The presence of the sidelobes in plot (b) makes it difficult to distinguish the real acoustic source distribution on the high frequencies. The map with F11S01 provides a clearer representation of the source distribution on the high frequencies.

It is instructive to examine the source distribution of Fig. 5.12 around the screech tone frequency. This is done in Fig. 5.13. As mentioned previously, the delay-and-sum noise source map (plot a) results in a low spatial resolution map compared to the other two. The Bayesian estimation with F12 (plot b) shows a spatially-periodic pattern of sources,

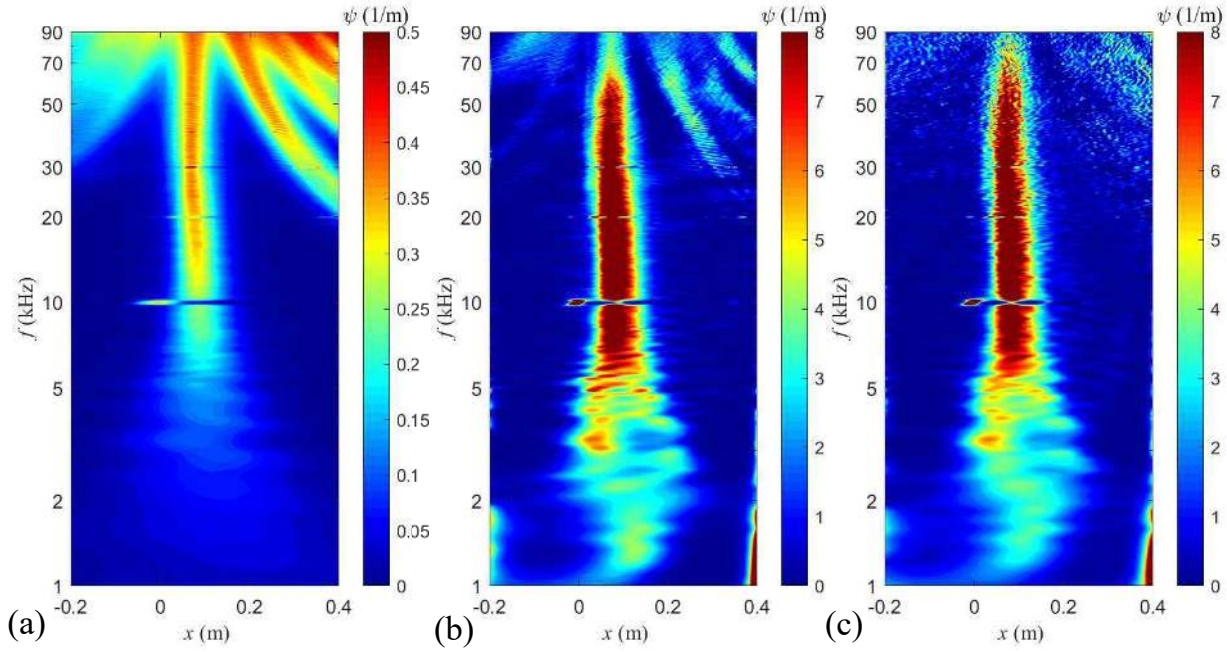

Figure 5.12: Coherence-based source strength $\psi(x, \omega)$ for the overexpanded jet using the full array configuration. (a) Delay-and-sum (F12); (b) Bayesian estimation (F12); (c) Bayesian estimation (F11S01)

corresponding to the screech generation and reflection, the strongest of those being near $x = 0$ m, where the plate is located. These features become sharper and more defined when using F11S01 (plot c). The generation of the screech tone near $x = 0.1$ m becomes better determined with F11S01.

Figure 5.14 shows two additional coherence-based noise source maps computed using the full array configuration and the Bayesian estimation method. Plots (a) and (b) correspond to F11S01 using the baseline block configuration and F11S01 using a block-patched noise source map, respectively (see Table 4.2). Both plots have been obtained by patching the results for different FFT sizes, as before. The figure shows how the presence of the sidelobes is reduced when using the proposed block distribution, resulting in a cleaner and sharper image. In terms of the frequency resolution, the source seems to be more "continuous" when computed with the developed signal segmentation and the high frequencies resolved are extended up to 90 kHz.

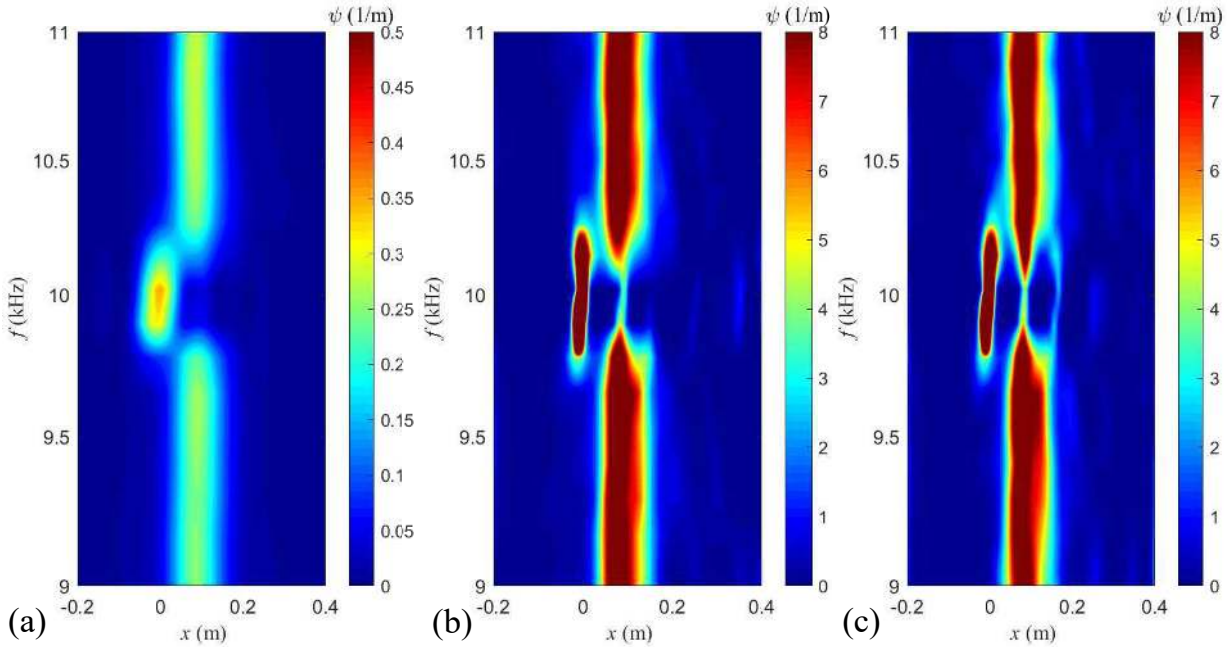

Figure 5.13: Detail of the coherence-based source strength $\psi(x, \omega)$ for the overexpanded jet using the full array configuration with the baseline block distribution of Ref. 1. (a) Delay-and-sum (F12); (b) Bayesian estimation (F12); (c) Bayesian estimation (F11S01) with the baseline block distribution.

The effect of the block segmentation is further assessed by showing a detail of the high frequencies. Figure 5.15 shows the acoustic source distribution for the high frequencies of the F11S01 with the baseline configuration (plot a) and F11S01 with the proposed signal segmentation (plot b). It can be seen how the spatial resolution increases considerably with the block-patched noise source map. This might be a direct consequence of the optimized block length that avoids information loss at the high frequencies.

The coherence of the acoustic field is analyzed, similarly to the Impinging Jets Source case, to assess the performance of the signal division.

The measured coherence of the acoustic field between microphone pairs for the overexpanded jet experiment is depicted in Fig. 5.16. It shows how as the frequency increases, the coherent envelope becomes sharper. In other words, high frequencies are only coherent for small distances while, on the other hand, low frequencies present longer coherent distances.

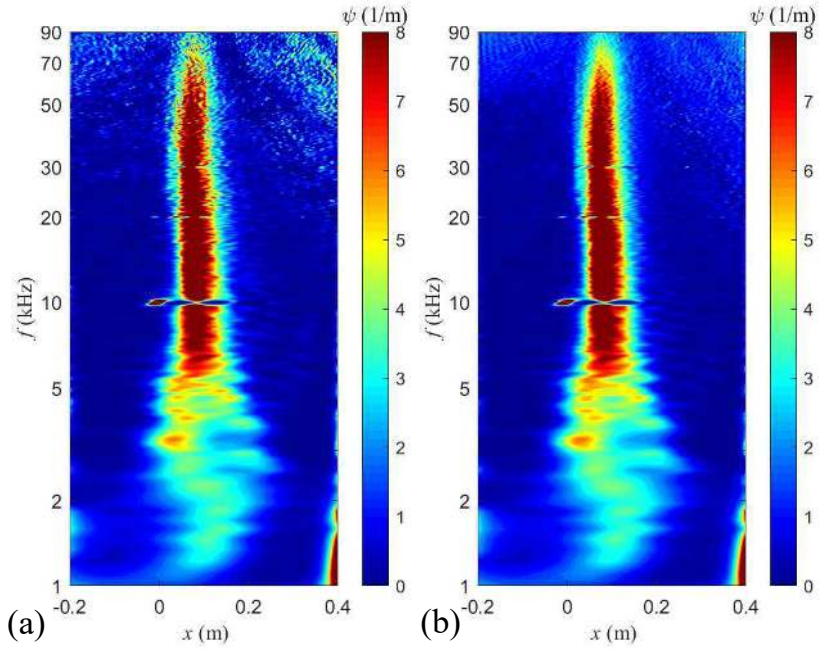

Figure 5.14: Coherence-based source strength $\psi(x, \omega)$ for the overexpanded jet using the full array configuration. (a) Bayesian estimation (F11S01) with the baseline block distribution of Ref. 1; (b) Bayesian estimation (F11S01) with the proposed block distribution.

The proposed signal segmentation naturally increases the total number of small distances between sensor pairs, as shown in Figs. 4.10, 4.11 and 4.12. This provides a huge advantage when resolving events with narrow spatial coherence, such as the ones presented in the over-expanded jet case. For these reasons, it is expected that the proposed signal segmentation will hugely benefit the resolution of the noise source maps when using a sparse microphone array. To this extent, additional figures are presented.

Figures 5.17 and 5.18 are presented to illustrate the benefits of the continuous scan approach when using an array configuration consisting in a reduced number of microphones.

Figure 5.17 shows three coherence-based noise source maps for the partial array configuration. The plots were obtained with the baseline block configuration when the scanning sensor was involved, in a similar way as before. The images (a), (b) and (c) were obtained similarly as those presented previously for the full array configuration. The delay-and-sum noise source

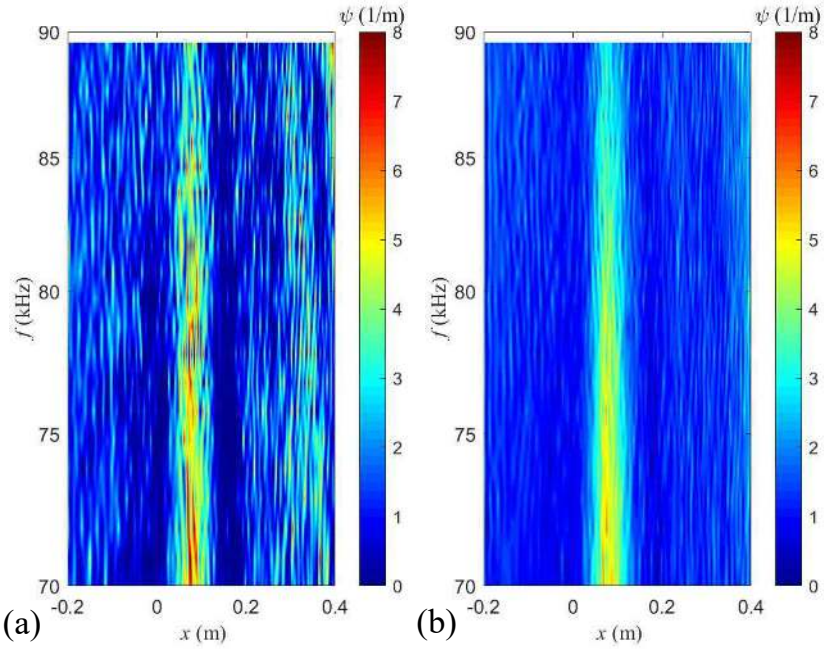

Figure 5.15: Detail of the coherence-based source strength $\psi(x, \omega)$ for the overexpanded jet using the full array configuration for the high frequencies. (a) Bayesian estimation (F11S01) with the baseline block distribution of Ref. 1; (b) Bayesian estimation (F11S01) with the proposed block distribution.

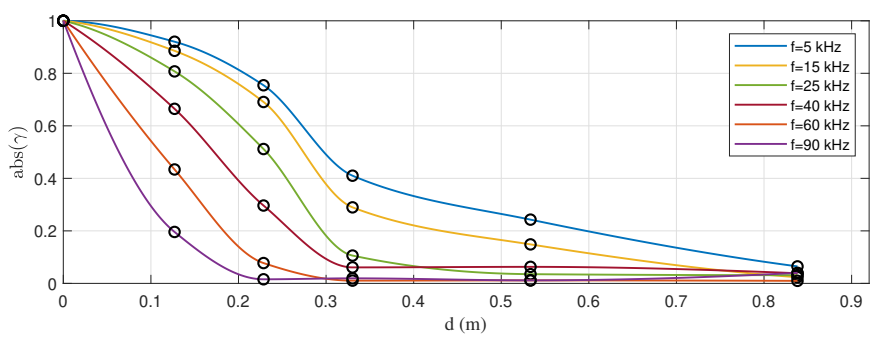

Figure 5.16: Measured coherence of the acoustic field for the Impinging Jets Source experiment as a function of the distance.

map is completely dominated by the sidelobes. The spatial resolution of the high frequencies is completely erased by the presence of the sidelobes. The delay-and-sum method provides a noise source map with little spatial resolution and in which it is difficult to identify the source. The screech reflection on the plate seems to be captured but additional sources appear due to the sidelobes for high x values. The Bayesian estimation with fixed sensors (F05) shows

an improvement with respect to the delay-and-sum map. The strength of the sidelobes is significantly reduced compared to the DAS. Nevertheless, the highest frequencies that are resolved reduce to about 30 kHz and its spatial resolution is relatively poor. In a similar way as the delay-and-sum map, the source blends with sidelobes. Finally, the acoustic source distribution obtained with F04S01 is better resolved in terms of spatial resolution and the resolved frequencies extend up to 80 kHz. The sidelobes are minimal for this configuration when compared to the other two noise source maps. Finally, it is seen how the acoustic source map of F04S01 has a similar quality to that of F11S01, expect for the acoustic source distribution loss at the high frequencies.

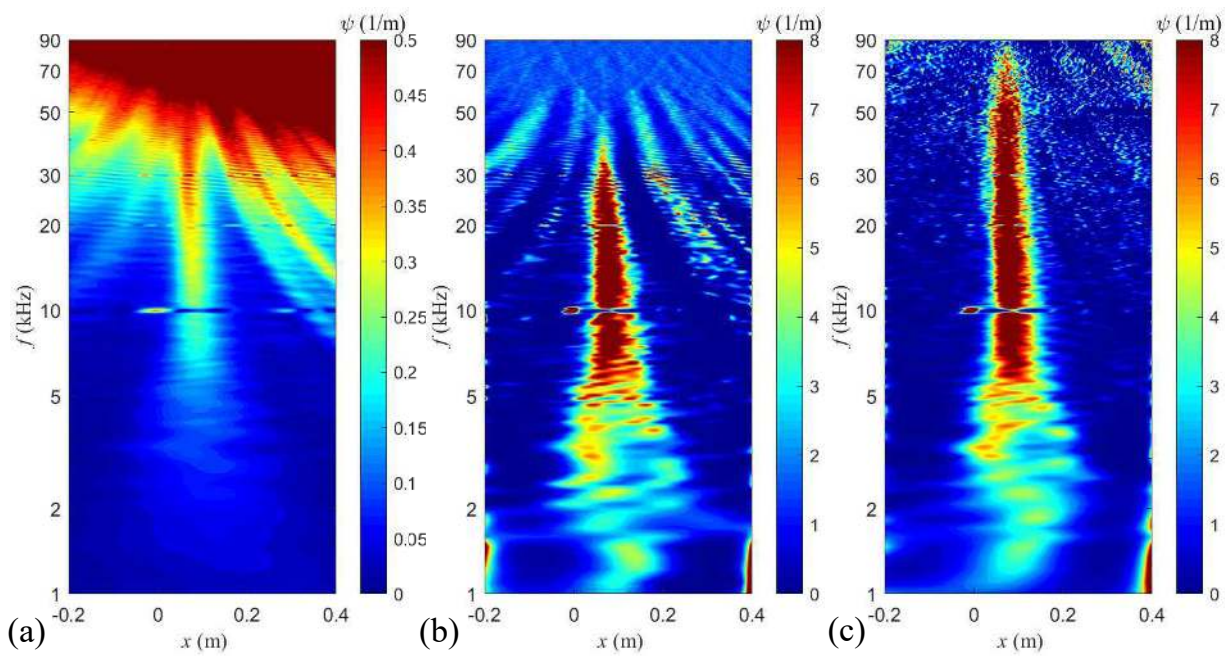

Figure 5.17: Detail of the coherence-based source strength $\psi(x, \omega)$ for the overexpanded jet using the full array configuration. (a) Delay-and-sum (F05); (b) Bayesian estimation (F05); (c) Bayesian estimation (F04S01) with the block distribution of Ref. 1

Figure 5.18 shows the detail of the noise source distribution near the screech tone. The delay-and-sum noise source map obtained when using the sparse array configuration shows a non-realistic source distribution near the screech tone due to the presence of the intense sidelobes. Bayesian estimation with F05 shows the presence of two ghost sources that could

be caused by the presence of the sidelobes as well. Finally, Bayesian estimation with F04S01 shows a noise source map that has a higher spatial resolution and in which the screech generation and reflection in the plate are well defined and comparable to F11S01.

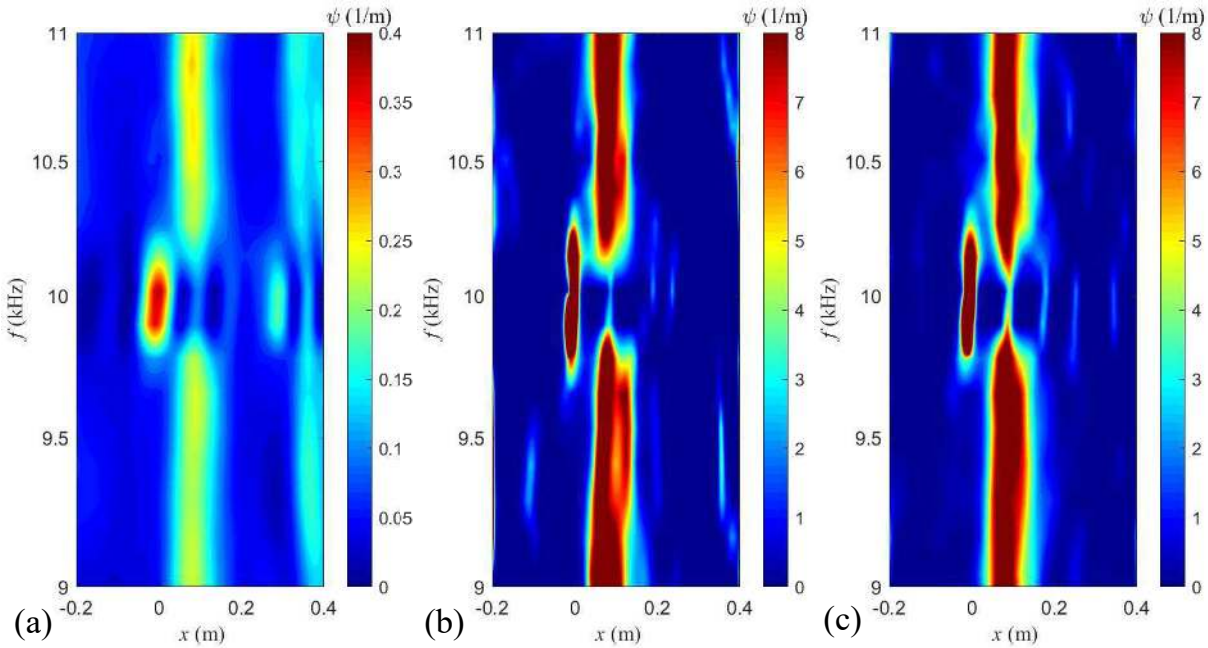

Figure 5.18: Detail of the coherence-based source strength $\psi(x, \omega)$ for the overexpanded jet using the full array configuration. (a) Delay-and-sum (F05); (b) Bayesian estimation (F05); (c) Bayesian estimation (F04S01) with the block distribution of Ref. 1

Figure 5.19 illustrates the benefits of the newly proposed signal segmentation when using a sparse microphone array to map complicated acoustic fields. Plots (a) and (b) correspond to F04S01 using the baseline block configuration and F04S01 using the block-patched noise source map, respectively (see Table 4.2). Both plots have been obtained by patching the results for different FFT sizes, similar as previously. The distance between sensor pairs is presented in Figs. 4.14, 4.15 and 4.16. It is shown how the dense block segmentation increases considerably the number of small distances between sensor pairs. The effect that this has on the high frequencies is also shown in the figures below.

The improved resolution of the high frequencies is particularly important when using a sparse array configuration. The segmentation of the signal into smaller blocks avoids information

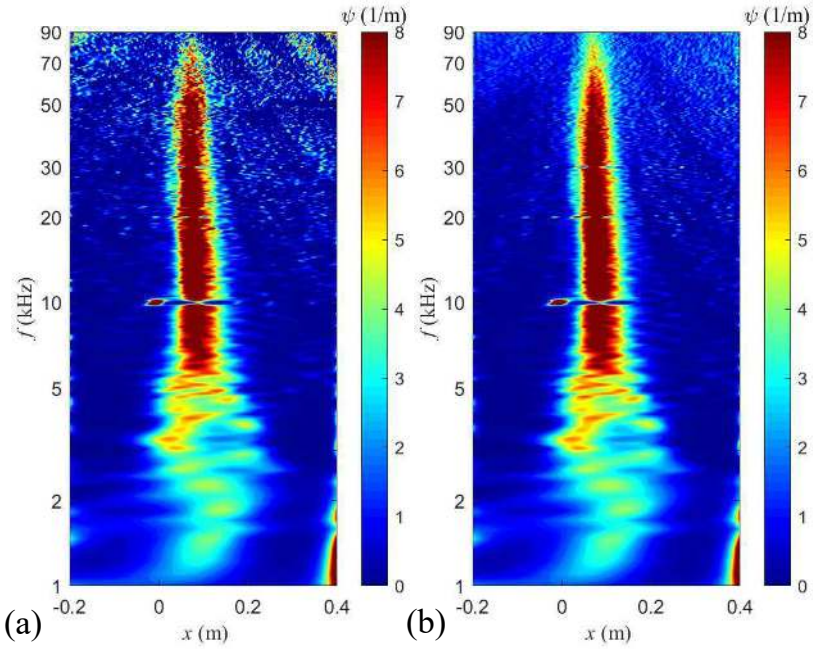

Figure 5.19: Coherence-based source strength $\psi(x, \omega)$ for the overexpanded jet using the partial array configuration. (a) Bayesian estimation (F04S01) with the baseline signal segmentation of Ref. 1; (b) Bayesian estimation (F04S01) with the proposed signal segmentation.

loss due to the frequency-dependent window and emphasizes the number of small distances between sensor pairs. This yields to a very high quality acoustic source distribution that is devoid of sidelobes and that shows a noise source with a similar quality to that obtained with F11S01 for the same block configuration. This is shown in Fig. 5.20.

Finally, Fig. 5.21 is presented to illustrate the benefits of the proposed signal segmentation, especially for the high frequencies. The image compares the distribution of the source computed with the full array configuration (F11S01) for plots (a) and (b), using different block distributions. Plot (c) was obtained with the partial array configuration and using the proposed signal segmentation. It can be seen how the proposed block distribution provides better results than the baseline block configuration, independent of the array geometrical configurations tested in this work.

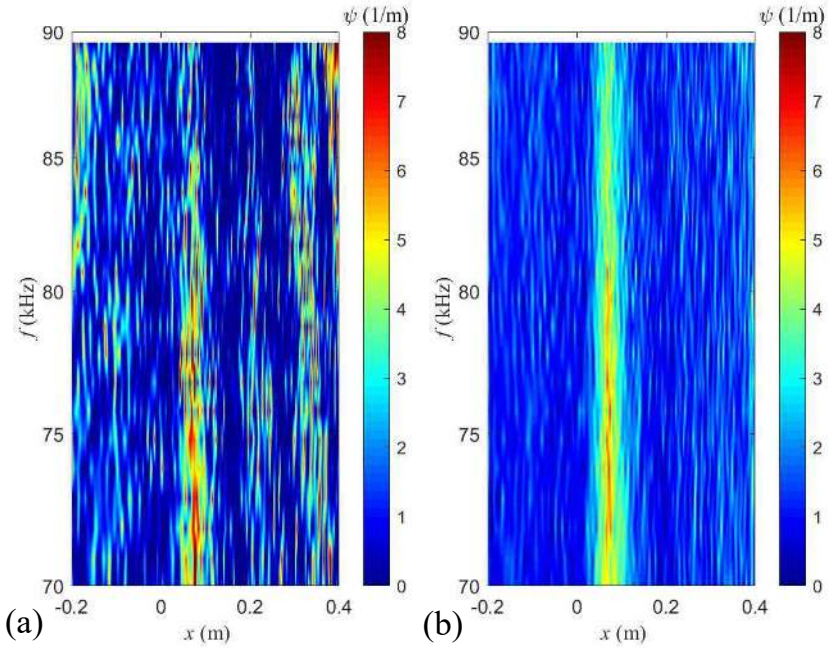

Figure 5.20: Detail of the coherence-based source strength $\psi(x, \omega)$ for the overexpanded jet using the partial array configuration for the high frequencies. (a) Bayesian estimation (F04S01) with the baseline block distribution of Ref. 1; (b) Bayesian estimation (F04S01) with the proposed block distribution.

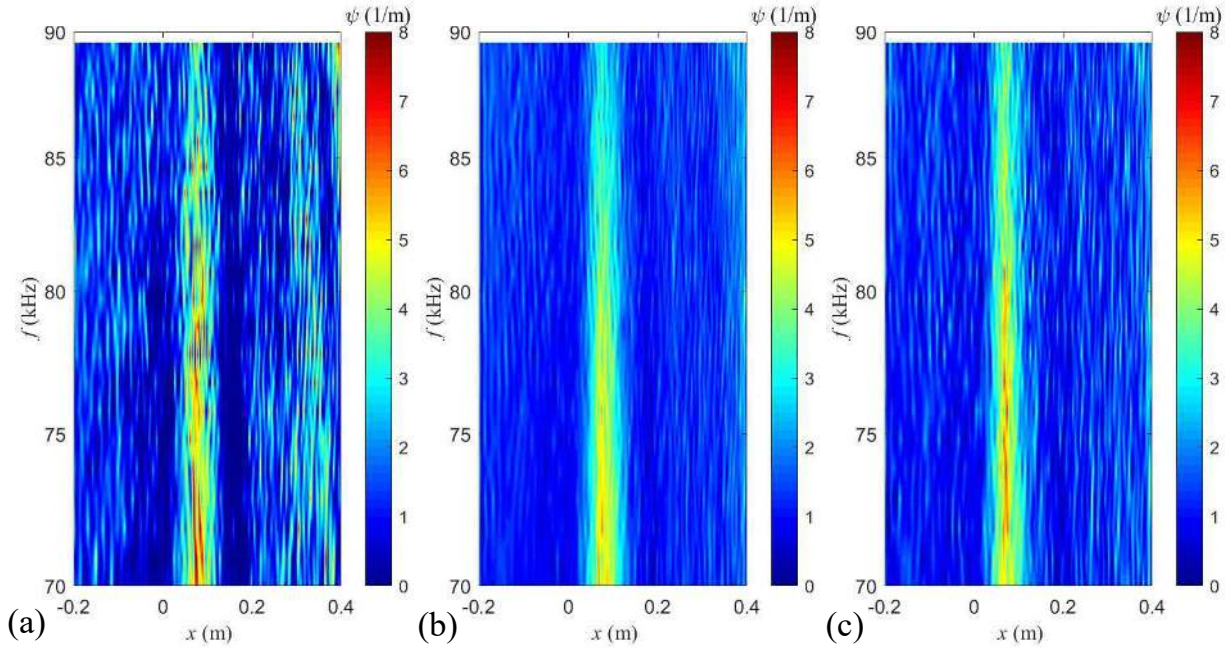

Figure 5.21: Detail of the coherence-based source strength $\psi(x, \omega)$ for the overexpanded jet.(a) Bayesian estimation (F11S01) with the baseline block distribution of Ref. 1; (b) Bayesian estimation (F11S01) with the proposed block distribution; (c) Bayesian estimation (F04S01) with the proposed block distribution

Chapter 6

Conclusion

6.1 Summary

The direct estimation of the spatio-spectral distribution of an acoustic source is estimated from measurements involving fixed and scanning sensors. A review of the methodology presented on the AIAA Journal paper[1] was presented in this thesis. The moving sensor introduced a non-stationarity on the the sensors' cross-correlation. The application of the Wigner-Ville spectrum allowed for a direct quantification and suppression of the non-stationarity. Suppression of the non-stationarity in the signal processing entails division of the signals into blocks and application of a frequency-dependent window within each block.

The signal segmentation was studied and a relation between the spectral parameters, the number of blocks and the block length was established. The block overlap was discussed as well. A curve relating block length and number of blocks that enclosed a "safe region" was determined. The effects of the frequency-dependent window were quantified in terms of the information loss depending on the frequency that was being resolved. This yielded to the determination of the optimal block distribution for a uniform signal segmentation.

The need for constructing noise source maps by patching the results for different block distributions and sizes of the Fast Fourier Transform depending on the frequency was discussed. Several noise source maps were presented to compare the proposed signal segmentation with a simpler block distribution (the baseline case of Ref. 1). The proposed signal segmentation yielded to histograms of distances between microphone pairs that emphasized the small distances. In addition, the discussed signal segmentation was shown to be more useful to accurately determine the envelope of the coherence of the acoustic field between microphone pairs. A dense block distribution benefited the spatial resolution of the high frequencies and improved considerably the imaging for arrays with fewer microphones.

The methodology was applied to acoustic fields emitted by impinging jets approximating a point source and an overexpanded supersonic jet. The measurement setup comprised one continuously scanning microphone and a number of fixed microphones, all arranged on a linear array. The noise source maps with the scanning microphone have improved spatial resolution and suppressed sidelobes. The proposed block distribution showed maps practically devoid of sidelobes and with an increased resolution when using the full array configuration (12 microphones). The advantage of the continuous scan paradigm was proven to be particularly strong when sparse microphone array configuration were used. The signal segmentation developed here proved to yield to maps with higher resolution and with weaker sidelobes. Noise source maps measured with only five sensors (four fixed and one scanning) had a similar quality and resolution to maps that were obtained with the full array configuration.

6.2 Recommendations for Future Work

The methodology and the experimental setup presented in this work could benefit from some additional improvements that could potentially increase the spatial resolution of the

high frequencies even more. Modifications and improvements on the code could reduce the processing time.

Improvements to the methodology include the experimentation with non-uniform block sizes and non-uniform block distributions. Further upgrade of the continuous-scan paradigm used here includes the use of variable scan speeds whereby the sensor slows down near regions of interest (for instance, regions in between two fixed microphones); the use of additional scanning sensors is might present additional improvements in the spatial resolution but new considerations will have to be made when suppressing the non-stationarity in the sensors' cross-correlations. The signal segmentation and block distribution might change with the use of additional scanning sensors.

Future research expectations include applying the continuous-scan paradigm to ducted fans and more complex nozzle designs.

Bibliography

[1] Papamoschou, D., Morata, D., and Shah, P., "Inverse Acoustic Methodology for Continuous-Scan Phased Arrays," *AIAA Journal*, 2019, pp. 1–16.

[2] Papamoschou, D., Morata, D., and Shah, P., "Direct Spectral Estimation Method for Continuous Scan Beamforming," *2018 AIAA/CEAS Aeroacoustics Conference, Paper 2018-2806*, 2018.

[3] Kish, C., *An Estimate of the Global Impact of Commercial Aviation Noise*, Master's thesis, Massachusetts Institute of Technology, 2008.

[4] Powell, A., "The Noise of Choked Jets," *The Journal of the Acoustical Society of America*, Vol. 25, No. 3, 1953, pp. 385–389.

[5] Tam, C. K. W., "Supersonic Jet Noise," *Annual Review of Fluid Mechanics*, Vol. 27, No. 1, 1995, pp. 17–43.

[6] Raman, G., "Advances in Understanding Supersonic Jet Screech : Review and Perspective," *Progress in Aerospace Sciences*, Vol. 34, No. 1-2, 1998, pp. 45–106.

[7] Tam, C. K. W., Parrish, S. A., and Viswanathan, K., "Harmonics of Jet Screech Tones," *AIAA Journal*, Vol. 52, No. 11, 2014, pp. 2471–2479.

[8] Norum, T. D., "Screech suppression in supersonic jets," *AIAA Journal*, Vol. 21, No. 2, 1983, pp. 235–240.

[9] Verma, S. B. and Rathakrishnan, E., "Flow and Noise Characteristics of Notched Elliptic-Orifice Jets," *Journal of Fluids Engineering*, Vol. 121, No. September, 1999, pp. 690–693.

[10] Abbey, E., *Directional Noise Suppresion in Dual-Stream High-Speed Jets*, Master's thesis, University of California, Irvine, 2002.

[11] Tam, C. K. W., Viswanathan, K., Ahuja, K. K., and Panda, J., "The sources of jet noise: experimental evidence," *Journal of Fluid Mechanics*, Vol. 615, 2008, pp. 253292.

[12] Tam, C., Golebiowski, M., and Seiner, J., "On the two components of turbulent mixing noise from supersonic jets," *2018 AIAA/CEAS Aeroacoustics Conference*, 1996.

[13] Viswanathan, K., "Analysis of the Two Similarity Components of Turbulent Mixing Noise," *AIAA Journal*, Vol. 40, No. 9, 2002, pp. 1735–1744.

[14] Johnson, D. H. and Dudgeon, D. E., *Array signal processing : concepts and techniques*, PTR Prentice Hall, Englewood Cliffs, New Jersey, 1st ed., 1993.

[15] Sarradj, E., "A Generic Approach To Synthesize Optimal Array Microphone Arrangements," *Proceedings of the 6th Berlin Beamforming Conference*, 2016, pp. 1–12.

[16] Arcondoulis, E. and Liu, Y., "An iterative microphone removal method for acoustic beamforming array design," *Journal of Sound and Vibration*, Vol. 442, 2019, pp. 552–571.

[17] Dougherty, R., "Extensions of DAMAS and Benefits and Limitations of Deconvolution in Beamforming," *AIAA Paper 2005-2961*, 05 2005.

[18] Papamoschou, D., "Imaging of directional distributed noise sources," *Journal of Sound and Vibration*, Vol. 330, No. 10, 2011, pp. 2265–2280.

[19] Lee, M. and Bolton, J. S., "Source characterization of a subsonic jet by using near-field acoustical holography," *The Journal of the Acoustical Society of America*, Vol. 121, No. 2, 2007, pp. 967–977.

[20] Vold, H., Shah, P., Davis, J., Bremner, P., and McKinely, R., "High-Resolution Continuous Scan Acoustical Holography Applied to High-Speed Jet Noise," 2010.

[21] Shah, P., Vold, H., and Yang, M., "Reconstruction of Far-Field Noise Using Multireference Acoustical Holography Measurements of High-Speed Jets," Tech. rep., AIAA Paper, 2011.

[22] Stephens, D. B. and Vold, H., "Order tracking signal processing for open rotor acoustics," *Journal of Sound and Vibration*, Vol. 333, 2014, pp. 3818–3830.

[23] Fernández Comesaña, D., Holland, K. R., García Escribano, D., and De Bree, H. E., "An introduction to virtual phased arrays for beamforming applications," *Archives of Acoustics*, Vol. 39, No. 1, 2014, pp. 81–88.

[24] Nicolas, F., "S1MA Wind Tunnel New Aeroacoustic Capability : a Traversing Microphone Array," *AIAA Paper 2018-3137*, 2018, pp. 1–14.

[25] Shanno, D. and Phua, K., "Minimization of Unconstrained Multivariate Functions," *ACM Transactions on Mathematical Software*, 1976, pp. 618–622.

[26] Leclère, Q., Pereira, A., Bailly, C., Antoni, J., and Picard, C., "A unified formalism for acoustic imaging based on microphone array measurements," *International Journal of Aeroacoustics*, Vol. 16, No. 4-5, 2017, pp. 431–456.

[27] Pereira, A., Antoni, J., and Leclère, Q., "Empirical Bayesian regularization of the inverse acoustic problem," *Applied Acoustics*, Vol. 97, 2015, pp. 11–29.

[28] Allen, J. B. and Rabiner, L. R., "A unified approach to short-time Fourier analysis and synthesis," *Proceedings of the IEEE*, Vol. 65, No. 11, Nov 1977, pp. 1558–1564.

[29] Martin, W. and Flandrin, P., "Wigner-Ville spectral analysis of nonstationary processes," *IEEE Transactions on Acoustics, Speech, and Signal Processing*, Vol. 33, No. 6, December 1985, pp. 1461–1470.

[30] Richardson, W., "Bayesian-Based Iterative Method for Image Restoration," *Journal of the Optical Society of America*, Vol. 62, No. 1, 1972, pp. 1–24.

[31] Lucy, L., "An Iterative Technique for the Rectification of Observed Distribubtions," *The Astronomical Journal*, Vol. 79, No. 6, 1974, pp. 745–754.

[32] Gerhold, C., Clark, L., Dunn, M., and Tweed, J., "Investigation of Acoustical Shielding by a Wedge-Shaped Airframe by," *Journal of Sound and Vibration*, Vol. 294, No. 1-2, 2004, pp. 49–63.

[33] Debiasi, M., *Acoustics of dual-stream high-speed jets*, Phd thesis, University of California, Irvine, 2000.